MERLIN, an adaptative LTE radiative transfer model for any mixture: Validation on Eurofer97 in argon atmosphere

Aurélien Favre, Arnaud Bultel, Vincent Morel, Morgan Lesage, Léo Gosse

Journal of Quantitative Spectroscopy & Radiative Transfer 330 (2025) 109222

Contents lists available at ScienceDirect

Journal of Quantitative Spectroscopy and Radiative Transfer

journal homepage: www.elsevier.com/locate/jqsrt

MERLIN, an adaptative LTE radiative transfer model for any mixture: Validation on Eurofer97 in argon atmosphere

Aurélien Favre *, Arnaud Bultel, Vincent Morel, Morgan Lesage, Léo Gosse

CORIA, UMR 6614, Université de Rouen Normandie, 76801 Saint-Etienne du Rouvray, France

ARTICLE INFO

Keywords:
Spectroscopy
Radiative transfer
Local thermodynamical equilibrium
Thermal plasma
Emission
Modeling
LIBS

ABSTRACT

Optical Emission Spectroscopy is used within the LIBS (Laser-Induced Breakdown Spectroscopy) technique to measure the elemental composition of a sample irradiated by a laser pulse. When the objective is to characterize a known alloy or to analyze the sample semi-quantitatively, standards can be used. This method refers to the "calibrated LIBS". When the studied sample is complex (for instance unknown alloy and/or concentration gradients), the modeling of the experimental emission spectra leads to the determination of the laser-induced plasma characteristics including its composition. This second method refers to the "calibration-free LIBS".

In this paper, we present the radiative transfer code MERLIN (MultiElemental Radiative equiLibrIum emissioN) aiming at matching experimental spectra of a laser-induced plasma in Local Thermodynamic Equilibrium (LTE) conditions for calibration-free LIBS. MERLIN provides the simulated spectra for any elementary mixture thanks to queries from spectral databases available online. The code is optimized and modular to allow outputs even for a high number of species.

The validation of MERLIN presented in the paper is based on a thorough analysis of the plasma emission performed on the alloy Eurofer97 in experimental conditions providing the LTE. The reconstruction of the observed spectra is performed with MERLIN. For the reconstruction, no adjusted variable is required since all the necessary parameters are derived from experiments.

1. Introduction

An emission spectrum corresponds to the evolution with wavelength of the spectral radiance, in other words the energy of the photons emitted per unit time, per unit emission surface area and per unit solid angle of emission. This evolution results from continuous and discrete radiative contributions. Each discrete contribution is characterized by a spectral profile convolving various broadening sources. In the literature related to laser-induced plasmas (LIP), many papers exploit these spectral profiles [1–3]. However, complete radiative transfer calculations [4] are rare. Although some tools are available [5,6], there are few validated simulation codes and they are mainly focused on redundant well-identified molecules [7–10].

Laser-Induced Breakdown Spectroscopy (LIBS) is a technique for determining the multi-elemental composition of a sample under gaseous, liquid or solid phase. To avoid any ambiguity resulting from the possible molecular systems observed, the atomic emission is analyzed. The most powerful way to quantitatively obtain the composition of the sample is to perform the experiments under Local Thermodynamic Equilibrium (LTE) conditions and to model the radiative signature of the analyzed plasma. Indeed under these equilibrium conditions, the excited states number density driving the emission coefficient only depends on the temperature local value. The cross comparison between experimental and simulated spectra leads to the determination of the composition of the sample. The resulting method is therefore called "calibration-free LIBS". As a result, in the following, the thermodynamic conditions will systematically correspond to equilibrium. The pressure level required then ranges over the interval $[10^2, 10^5]$ Pa [11].

Since this approach is based on LTE, the capacity of calculating a relevant composition with respect to the thermodynamic conditions plays a crucial role. Thermodynamic database have therefore to be sufficiently complete and accurate. The profile of the lines being affected by numerous broadening effects, their calculation also requires databases sufficiently complete. Moreover, the radiance of the lines can be sensitive to self-absorption resulting from a lower state of the concerned transition with a too high population number density. A realistic calculation of the spectra then requires the application of the Radiative Transfer Equation (RTE).

* Corresponding author.
E-mail address: aurelien.favre@coria.fr (A. Favre).
URL: http://www.coria.fr (A. Favre).

https://doi.org/10.1016/j.jqsrt.2024.109222
Received 29 July 2024; Received in revised form 8 October 2024; Accepted 11 October 2024
Available online 18 October 2024

In the present paper, the MERLIN (MultiElemental Radiative equi-LibrIum emissioN) code is presented. This code is based on the treatment of the RTE. The development of this code has been motivated by the need for exploiting the calibration-free LIBS to characterize the composition of complex samples [12–16]. MERLIN is built to be a versatile, autonomous and flexible tool. The versatility lies in the wide range of mixtures treated. Indeed, any monatomic mixture, without limit on the number of species, can be considered by automated generation of a system of differential equations governing a fictitious chemistry of the mixture leading to the composition at LTE. Polyatomic species is supported and functional but is not presented in the paper. The autonomy of the code lies in its ability to query several freely accessible online databases and to perform multi-base calculations. Finally, the flexibility of use provided by parallelization and optimization by vectorization makes it possible to carry out a simulation on machines with low computing capacities.

In the upcoming sections, the theoretical background of the code and the validation experiments are successively described.

2. Theoretical background

The reader is invited to refer to Tables A.1–A.3 in appendices for the notations used in the following.

2.1. Equilibrium composition calculation

Complete thermodynamic equilibrium is never fully satisfied in a plasma [17]. Indeed, it imposes the microreversibility of each elementary process (collisional and radiative) while some of these processes are fundamentally irreversible (for instance spontaneous emission). It also requires that no loss of energy occurs at the periphery of the plasma. The concept of LTE requires low local gradients and the predominance of collisional processes in plasma kinetics. The relaxation of an isolated system as collisions occur, neglecting radiative losses, leads to a stationary state which corresponds to the equilibrium. This equilibrium is thermochemical. Indeed, the translation velocities of each constituent correspond to the Maxwellian distribution at the same temperature and the chemical composition is stable with given ionization and dissociation degrees. This equilibrium is unique for a given mixture under given thermodynamic conditions. These characteristics are used to derive the equilibrium composition of any mixture of elements, provided the relevant databases are available.

2.1.1. Adaptive generation of a coupled system

The MERLIN code is elaborated to support automatically very rich mixtures. The list of the elements and their mole fraction is given. The species within the plasma are generated numerically using an approach based on regular expressions (*regex* and *pattern matching*). Only the species X are then taken into consideration if the partition functions $Q_X(T)$ and the ionization potentials E_{io} and/or dissociation E_{di} are known. A list of fictitious reactions is then automatically generated. This involves identifying for each species whether it is part of the reactants or the products for each reaction. Of course, some species are reactants for one reaction and products for another reaction. This results in a coupling necessary for the resolution. The automatically generated reactions are ionization or dissociation reactions because they allows the distribution of elements in molecules and ions. Therefore a typical fictitious process can be written as

$$R + M \underset{k_b}{\overset{k_f}{\rightleftarrows}} P_1 + P_2 + M \tag{1}$$

with R, M, P_1 and P_2 are a reactant, a collision partner and arbitrary products, respectively. The k_f and k_b rate coefficient drive the forward and backward processes. Since the equilibrium constant $K_{eq} = \frac{n_{P_1} n_{P_2}}{n_R}$ with n_{P_1}, n_{P_2} and n_R are the number density in P_1, P_2 and R respectively, we have

$$K_{eq} = \frac{k_f}{k_b} \tag{2}$$

The system of coupled temporal differential equations is generated from the elements of the mixture. Each of them corresponds to the balance equation of the number N of each component. In the case of the example (1), this system will be written

$$\begin{cases} \dfrac{dN_R}{dt} = k_f \left(-N_R + \frac{1}{K_{eq}} N_{P_1} n_{P_2} \right) n_M & \text{(a)} \\ \dfrac{dN_{P_1}}{dt} = -\dfrac{dN_R}{dt} & \text{(b)} \\ \dfrac{dN_{P_2}}{dt} = -\dfrac{dN_R}{dt} & \text{(c)} \end{cases} \tag{3}$$

The value of k_f can be arbitrarily chosen without any impact on the values of n_R, n_{P_1} and n_{P_2} once the steady-state has been reached. Depending on the mixture considered, several hundred coupled differential equations can be generated for the LTE composition computation. It should be noted that the previous approach solving this kinetic problem is strictly equivalent to the one based on the Gibbs energy minimization [18].

2.1.2. Ionization potential lowering and mass action laws

The electric field due to the charged particles as well as the collisions with the free electrons lead to a modification of the atomic energy levels within the plasma. The partition functions are then perturbed at high temperatures. The classical approach considers an ionization potential lowering. This correction can be determined using detailed models of atomic structure. The most widespread approach is that of Stewart and Pyatt [19]. Several simplified analytical forms are proposed in the literature. The form due to Unsöld et al. [20] involves the ionization potential of H and the Bohr radius to take into account only the closest ions. Ecker and Kröll [21] propose a more general form depending on the Debye length. We have considered the approach proposed by Griem [22]. For weakly ionized plasmas, the ionization potential lowering is approximated by

$$\Delta E_{io}\ [\text{eV}] = \frac{Ze^2}{4\pi\epsilon_0} \sqrt{\frac{(Z+1)}{\epsilon_0 k_B} \frac{n_e\ [\text{m}^{-3}]}{T\ [\text{K}]}} \tag{4}$$

In the context of laser-induced plasmas, the ionization potential lowering is of the order of a few 10^{-2} eV. We then define E_{io}^c as being the corrected ionization energy such as

$$E_{io}^c = E_{io} - \Delta E_{io} \tag{5}$$

Since ionization and dissociation are driven by similar equilibrium constants, the equilibrium constant for process (1) is generalized under the form

$$K_{eq} = \frac{Q_{P_1} Q_{P_2}}{Q_R} \left(\frac{2\pi\mu k_B T}{h^2} \right)^{\frac{3}{2}} \exp\left(-\frac{\delta_{r,io}\, E_{io}^c(R) + \delta_{r,di}\, E_{di}(R)}{k_B\, T} \right) \tag{6}$$

with μ the reduced mass between P_1 and P_2. The Kronecker symbols $\delta_{r,io}$ and $\delta_{r,di}$ make it possible to associate the appropriate potentials with each reaction r considered. It is important to mention that the partition functions are calculated assuming no density dependence. Globally, this is equivalent to not taking into account a Virial or Debye Huckel correction to the equation of state.

2.1.3. Fictitious kinetics

As mentioned, an arbitrary value of k_f is taken. The temperature level T is chosen. The resolution of the system of equations is done once chosen the state equation. Prenzel et al. [23] have shown that the ideal gas equation of state is relevant for the thermodynamic conditions $T \lesssim 10^5$ K and $n_e \lesssim 10^{27}$ m^{-3}. These conditions are those of the

laser-induced plasmas. This equation of state is therefore used. Two resolution procedures can be chosen.

Resolution for constants (T, p)

The chemical kinetics being fictitious, the reaction (1) is assumed to be independent of the type of the collision partner. This means that all collision partners play the same role. We thus write that the density in M corresponds to the total plasma density n_{tot}

$$n_M = \sum_X n_X = n_{tot} \tag{7}$$

Then, from the ideal gas equation of state

$$n_{tot} = \frac{p}{k_B T} \tag{8}$$

The forward reaction rate is chosen with respect to an arbitrary characteristic resolution time τ_{res} set to 1 second such as

$$k_f = \left(\tau_{res}\, n_{tot}\right)^{-1} \tag{9}$$

To keep pressure p constant when dissociation, ionization or recombination take place, the plasma volume defined as

$$V(t) = \frac{1}{n_{tot}} \sum_X N_X(t) \tag{10}$$

must temporally evolve. Then Eq. (3)**a** can be rewritten as

$$\frac{dN_R(t)}{dt} = \frac{1}{\tau_{res}} \left(-N_R(t) + \frac{1}{K_{eq}} \frac{N_{P_1}(t)\, N_{P_2}(t)}{V(t)} \right) \tag{11}$$

and is finally solved.

Resolution for constants (T, n_X)

The resolution can also be done at fixed n_X. Then

$$n_M = n_X \tag{12}$$

and the forward reaction rate is

$$k_f = \left(\tau_{res}\, n_X\right)^{-1} \tag{13}$$

The plasma volume is therefore

$$V(t) = \frac{N_X}{n_X} \tag{14}$$

and Eq. (11) can be solved.

This last approach is particularly appropriate to the study of laser-induced plasmas. Indeed, since electron density n_e is usually derived directly from the Stark broadening of optically thin lines with a relatively high degree of accuracy, calculating the composition in fixed (T, n_e) conditions is relevant.

2.1.4. Benchmark comparison

Fig. 1 displays the evolution of the composition of an ideal mixture at $p = 10^5$ Pa of dry air (mole fraction 0.2115 for O_2 and 0.7885 for N_2) as a function of T. Ionization energies and partition functions for monatomic species are taken from the NIST database [24]. The ionization and dissociation energies as well as the polyatomic partition functions are due to Capitelli et al. [25]. The species O_2^-, O^- and NO^- were neglected in the calculation owing to their rather low detachment energy, which leads to very weak densities at several thousand of K [26]. The figure also displays reference calculations [27–29]. One can see that the MERLIN outputs are in good agreement with them. None of the sources allows a comparison with the N_2O^+ density obtained by MERLIN, whose values are very weak. We can notice some discrepancies for $T < 3000$ K for NO and NO_2. They are due to differences in the partition function of NO_2 which impacts the density in NO owing to the mass action law coupling O, NO and NO_2.

2.2. Radiative transfer

Although the following equations are presented as a function of the wavelength λ, the calculations are actually performed as a function of the frequency $\nu = c/\lambda$. They correspond to constant energy steps and thus to a more realistic spectral dispersion.

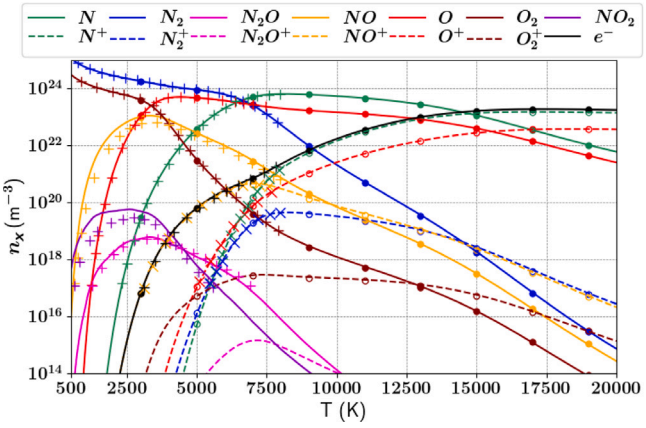

Fig. 1. Evolution of the LTE composition of a mixture (0.2115 O_2, 0.7885 N_2) at $p = 10^5$ Pa as a function of T. MERLIN outputs are shown in solid lines for neutral and dotted lines for charged species. The results of [27–29] are indicated by circles and crosses.

2.2.1. Treatment of the Radiative Transfer Equation

The general RTE is written

$$\frac{1}{c}\frac{\partial L_\lambda}{\partial t} + \frac{\vec{e}}{c}.\vec{\nabla} L_\lambda = \epsilon_\lambda - \left(\alpha_\lambda + \delta_\lambda\right) L_\lambda + \frac{\delta_\lambda}{4\pi} \int_{\Omega_1} \Psi_\lambda(\vec{\Omega_1}, \vec{\Omega_2}) L_\lambda \, \mathrm{d}^2\Omega \tag{15}$$

with classical notations and with L_λ the spectral radiance (expressed in W m^{-2} sr^{-1} m^{-1}). The plasma studied is assumed to be weakly diffusive and at steady-state. In the one-dimensional case (x-coordinate), the RTE (15) reduces to

$$\frac{dL_\lambda}{dx} = \epsilon_\lambda - \alpha_\lambda L_\lambda \tag{16}$$

with the emission ϵ_λ and absorption α_λ coefficients. At equilibrium, the spectral radiance is uniform ($\frac{dL_\lambda}{dx} = 0$) and we can write $L_\lambda = L^0_{\lambda,T}$ with $L^0_{\lambda,T}$ the Black Body (BB) spectral radiance at temperature T given by

$$L^0_{\lambda,T} = \frac{2hc^2}{\lambda^5} \frac{1}{\exp\left(\frac{hc}{\lambda k_B T}\right) - 1} \tag{17}$$

The simplified RTE (16) then leads to the Kirchhoff's law

$$\epsilon_\lambda = \alpha_\lambda L^0_{\lambda,T} \tag{18}$$

The simplified RTE (16) then writes as

$$\frac{dL_\lambda}{dx} = \alpha_\lambda (L^0_{\lambda,T} - L_\lambda) \tag{19}$$

Fig. 2 illustrates the general physical situation, the simplification and the relevant boundary conditions. Due to the existence of gradients along the x-axis (sub Fig. 2**a**), the plasma is cut in N layers at LTE, each one having a thickness ℓ_k (sub Fig. 2**b**). Assuming the absence of radiation coming from outside the plasma along the x-axis, the integration of the simplified RTE (19) leads to the last layer spectral radiance

$$L_{\lambda_N} = L^0_{\lambda,T_N}\left(1 - e^{-\alpha_{\lambda_N}\ell_N}\right) + \sum_{k=1}^{N-1} L^0_{\lambda,T_k}\left(1 - e^{-\alpha_{\lambda_k}\ell_k}\right) e^{-\sum_{i=k+1}^{N} \alpha_{\lambda_i}\ell_i} \tag{20}$$

Let us simplify the approach by considering only $N = 2$ layers (sub Fig. 2**c**). This simplification corresponds well to the case of a uniform core plasma (with the thickness ℓ_1) surrounded by a colder layer (with the thickness ℓ_2). Eq. (20) is then reduced to

$$L_{\lambda_{N=2}} = L^0_{\lambda,T_2}\left(1 - e^{-\alpha_{\lambda_2}\ell_2}\right) + L^0_{\lambda,T_1}\left(1 - e^{-\alpha_{\lambda_1}\ell_1}\right) e^{-\alpha_{\lambda_2}\ell_2} \tag{21}$$

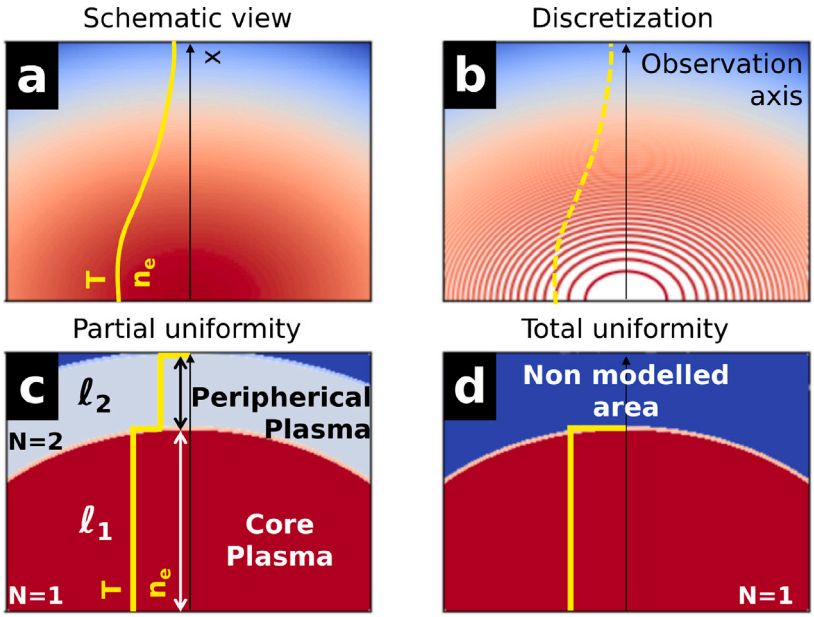

Fig. 2. Schematics of the geometry and profiles of (T, n_e) considered for the modeling of a laser-induced plasma in MERLIN. **a**: Indicative visual of the physical situation; **b**: Conceptual visual of an infinitesimal discretization; **c**: Geometry adopted for piecewise homogeneity; **d**: Homogeneous plasma boundary condition (unmodeled cold layer).

The modeling of the emission by a uniform plasma (sub Fig. 2**d**) can be obtained by considering either the thickness ℓ_2 of the cold layer equal to zero or the emission coefficient (therefore the absorption coefficient α_{λ_2}) equal to zero such as

$$L_{\lambda_1} = L_{\lambda,T_1} = L^0_{\lambda,T_1}\left(1 - e^{-\alpha_{\lambda_1}\ell_1}\right) = \frac{\epsilon_{\lambda_1}}{\alpha_{\lambda_1}}\left(1 - e^{-\alpha_{\lambda_1}\ell_1}\right) \tag{22}$$

When the product $\alpha_{\lambda_1}\ell_1 \ll 1$, the plasma can be qualified as "optically thin" and Eq. (22) is then simplified using a Taylor series in

$$L_{\lambda,T_1} = \epsilon_{\lambda_1}\ell_1 \tag{23}$$

2.2.2. Free-bound/free-free emission

Continuous radiation is due to free electrons. The contributions to the emission of the free-bound (radiative recombination, superscript fb) and free-free (thermal Bremsstrahlung, superscript ff) processes [30] are taken into account.

The emission coefficient for radiative recombination is

$$\epsilon^{fb}_{\lambda,X^{(Z+)}} = Z^2\frac{C_1}{\lambda^2}\frac{g_0^{X^{(Z+)}}}{Q_{X^{(Z+)}}}\frac{n_e n_{X^{(Z+)}}}{\sqrt{T}}\left[1 - \exp\left(-\frac{hc}{\lambda k_B T}\right)\right]\xi^{fb}(\lambda,T,Z) \tag{24}$$

The emission coefficients for thermal Bremsstrahlung are

- for electron - ion interactions (superscript ei):

$$\epsilon^{ff,ei}_{\lambda,X^{(Z+)}} = Z^2\frac{C_1}{\lambda^2}\frac{n_e n_{X^{(Z+)}}}{\sqrt{T}}\exp\left(-\frac{hc}{\lambda k_B T}\right)\xi^{ff}(\lambda,T,Z) \tag{25}$$

- for electron - neutral atom interactions (superscript ea):

$$\epsilon^{ff,ea}_{\lambda,X} = \frac{C_2}{\lambda^2}n_e n_X \sigma_{ea}(T)\sqrt{T^3}\left[\left(1 + \frac{hc}{\lambda k_B T}\right)^2 + 1\right]\exp\left(\frac{hc}{\lambda k_B T}\right) \tag{26}$$

In Eqs. (24) to (26), the universal constants C_1 and C_2 are respectively defined by [31]

$$C_1 = \frac{16\pi\left(\frac{e^2}{4\pi\epsilon_0}\right)^3}{3c^2\sqrt{6k_B\pi m_e{}^3}} \tag{27}$$

$$C_2 = \frac{32k_B\pi^2}{3h^4c^4\sqrt{3}}\left(\frac{e^2}{4\pi\epsilon_0}\right)^3 \tag{28}$$

$g_0^{X^{(Z+)}}$ is the degeneracy of the fundamental state of the ion $X^{(Z+)}$. We note $\xi^{fb}(\lambda,T,Z)$ and $\xi^{ff}(\lambda,T,Z)$ the Bibermann factors (extension of the Gaunt factor to non-hydrogenlike atoms) respectively for free-bound and free-free interactions. Finally, $\sigma_{ea}(T)$ is the mean electron-neutral elastic cross-section.

The total contribution of continuous radiation to the emission coefficient for element X is the sum of free-bound and free-free emission coefficients

$$\epsilon^{cont}_{\lambda,X} = \epsilon^{fb}_{\lambda,X^{(Z+)}} + \epsilon^{ff,ei}_{\lambda,X^{(Z+)}} + \epsilon^{ff,ea}_{\lambda,X} \tag{29}$$

Fig. 3 illustrates the relative contributions of $\epsilon^{fb}_{\lambda,X^{(Z+)}}$, $\epsilon^{ff,ei}_{\lambda,X^{(Z+)}}$ and $\epsilon^{ff,ea}_{\lambda,X}$ for Ar, Ar^+ and Ar^{2+} with respect to the full continuous emission coefficient defined by Eq. (29). This plot results from the composition of a pure argon plasma at LTE in the conditions (T, p) = (13 500 K, 4×10^5 Pa). In these thermodynamic conditions typical for LIP, we notice that the contribution of the Ar^+/Ar radiative recombination is predominant, followed by the contribution of Bremsstrahlung of Ar^+ and Ar. The contributions resulting from multi-charged ions are 3 to 5 orders of magnitude lower. Despite these weak contributions, no one is neglected for the computation of the continuum by MERLIN.

The literature does not provide the values of $\xi^{fb}(\lambda,T,Z)$ and $\sigma_{ea}(T)$ for each species. Therefore, we have assumed that averaged values related to the case of pure argon (ideal hydrogenlike mixture) are representative. Figs. 4 and 5 display the values given by the literature (reviews of Wilbers et al. [30] and Devoto [32], respectively). The retained values are therefore $\xi^{fb}(\lambda,T,Z) = 1.75$ and $\sigma_{ea}(T) = 3\times10^{-19}$ m^2, even if they rapidly present limitations when non-hydrogenlike species are taken into account. Additionally, we set $\xi^{ff}(\lambda,T,Z) = 1$ according to the Sutherland charts [33].

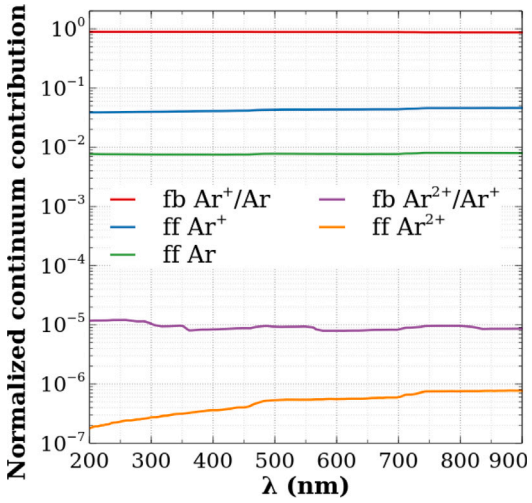

Fig. 3. Relative contributions of radiative recombination and thermal Bremsstrahlung for a monatomic mixture (Ar, Ar^+, Ar^{2+}, e^-) at LTE for (T, p) = (13500 K, 4×10^5 Pa) [30].

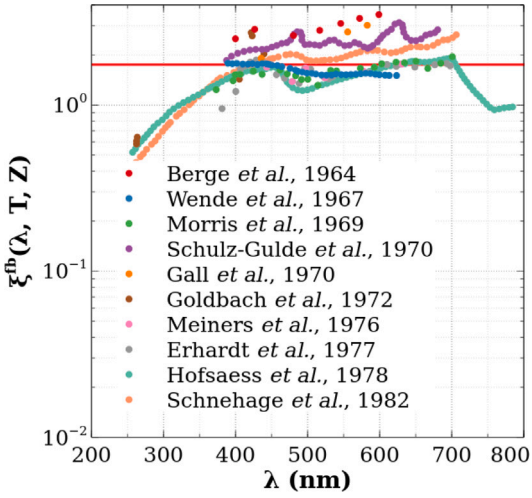

Fig. 4. Experimental and theoretical free-bound Bibermann factors for an argon plasma ($12\,000 < T(\mathrm{K}) < 14\,500$). We refer the reader to the work of Wilbers et al. [30] for the associated references. The red line corresponds to the value considered in MERLIN.

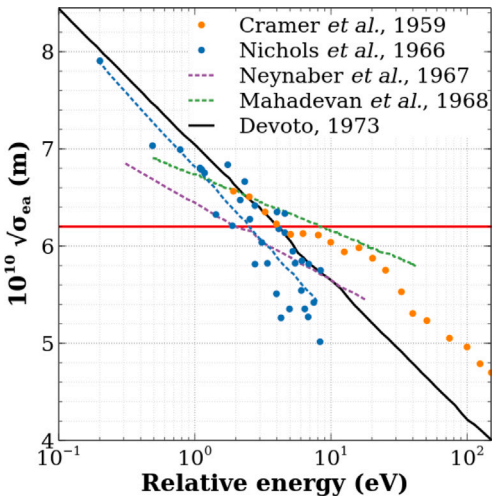

Fig. 5. Electron-neutral interaction cross sections for an argon plasma. This graph is taken from the work of Devoto, so we refer the reader to his paper for the associated Refs. [32]. The red line corresponds to the value considered in MERLIN.

2.2.3. Bound-bound emission

The population of excited states at LTE is governed by the Boltzmann statistics. Thus, for the species X, the population density $[X_k]$ of an emitting level k is related to the total density at equilibrium $n_X(\mathrm{eq.}) = \sum_k [X_k]$ by

$$[X_k] = \frac{g_k}{Q_X} \exp\left(-\frac{E_k}{k_B T}\right) n_X(\mathrm{eq.}) \tag{30}$$

The contribution of a transition $k \rightarrow i$ by spontaneous deexcitation to the emission coefficient is then given by

$$\epsilon^{ki}_{\lambda,X} = \frac{hc}{4\pi} \frac{A_{ki}\,[X_k]}{\lambda_{ki}} \Gamma(\lambda) \tag{31}$$

with $\Gamma(\lambda)$ the spectral profile such as $\int \Gamma(\lambda)\,\mathrm{d}\lambda = 1$. For each transition and for each species of the mixture, the calculation of $\epsilon^{ki}_{\lambda,X}$ is carried out. Depending on the radiative data considered, the transitions taken into account are more or less numerous and the radiance of the resulting lines can be modified.

The contribution of each species to the emission coefficient at wavelength λ has to be summed with other contributions such as

$$\epsilon_{\lambda,X} = \epsilon^{cont}_{\lambda,X} + \sum_{ki} \epsilon^{ki}_{\lambda,X} \tag{32}$$

The final emission coefficient considered in the radiative transfer equations of Section 2.2.1 is then the sum of all the contributions (continuous and discrete) of each species

$$\epsilon_\lambda = \sum_X \epsilon_{\lambda,X} \tag{33}$$

2.2.4. Spectral profile

The observed spectra result from the convolution of the spectral profile $\Gamma(\lambda)$ due to several physical phenomena with pure optical effects. These contributions being Gaussian and Lorentzian, their convolution leads to a hybrid Voigt profile. In an optimized approach, the resulting profile is approximated (deviation $< 1\%$ compared to a convolved Voigt profile) by a pseudo-Voigt polynomial law [34–37]. The MERLIN calculation is parallelized. It is therefore not easy to precisely evaluate the gain in terms of execution time obtained by the use of this pseudo-Voigt approximation. Nevertheless, a comparison has been performed. We have used a classical computer equipped with 12 *threads* and we have modeled the emission of tungsten (including W, W^+, e^-) on the spectral range [300, 800] nm with a spectral resolution of $\Delta\lambda = 10^{-2}$ nm ($\approx$ 65000 points). In these conditions, around 4200 transitions listed in the DESIRE database [38] are taken into account involving most of the causes of broadening described below. The execution time using a pseudo-Voigt approximation is $\approx$ 10 s while the calculation requires $\approx$ 60 min using a direct convolution procedure. This comparison is just an illustration and cannot be extrapolated, the execution time being a highly non-linear function of the total number of transitions. The gain obtained by the approximation is nevertheless significant.

2.2.5. Broadening sources

First, the broadening associated to the observation equipment leading to the apparatus function is taken into account. Indeed, the observation of a monochromatic source or low pressure spectral emission reveals a line profile whose broadening varies according to the width f_e of the entrance slit of the spectrometer. Our equipment generates a Lorentzian broadening with a Full Width at Half Maximum (FWHM) noted $\Delta\lambda^A_{1/2,L}$.

Second, numerous physical phenomena lead to line broadening. They are rapidly described below and discussed after.

- The natural broadening is caused by the lifetime of an atom or an ion on its excited state. This broadening is Lorentzian and depends on the probability per unit time of spontaneous emission (Einstein coefficient). For the Lyman-α transition of hydrogen, its contribution is estimated to 10^{-8} nm [39]. This broadening is estimated to 5.4×10^{-6} nm for the O I triplet at 777.3 nm [40]. An analytical form is given by Kelleher for the visible radiation of He [41].
- The collective effect, also called *high frequency Stark effect* due to oscillations of the electric field within the plasma, can lead to a Lorentzian broadening ascribed to turbulence. This effect becomes significant for particularly dense plasmas [39].
- The effect of an external magnetic field (Zeeman effect), leads to a modification of the energy levels driven by the intensity in the magnetic field and the relative orientation of the angular momentum. The line is then broadened. A similar effect takes place under external electric field and is a Stark effect.
- The broadening of absorption (or opacity broadening) is ascribed to several phenomena that can cause a modification of the profile. Among these, absorption by cold edges (see Section 2.2.1) or overpopulation of a level with respect to equilibrium [42] are the most cited. For O I triplet at 777.3 nm, this broadening is $\sim 10^{-8}$ nm [40].
- The Doppler broadening is due to the motion of emitters. Indeed, the relative speed with respect to the spectrometer causes the modification of the wavelength of the radiation emitted by the atoms and ions which collectively leads to a broadening whose Gaussian FWHM is [42]

$$\Delta\lambda^{D}_{1/2,G} = \lambda_{ki}\sqrt{8\,\ln 2\,\frac{k_B\,T}{m_k\,c^2}} \tag{34}$$

- The resonance broadening occurs when an atom emitting a photon for which the upper level of the concerned transition is coupled with the ground state interacts with an identical atom whose ground state is also populated. The associated Lorentzian FWHM is given by

$$\Delta\lambda^{R}_{1/2,L} = \frac{3e^2}{16\pi\,\epsilon_0\,m_e\,c^2}\,{\lambda_{ki}}^2\,\lambda_{i0}\,f_{0i}\,[X_0]\sqrt{\frac{g_0}{g_i}} \tag{35}$$

  with usual variables.
- The neutral pressure broadening (or Van Der Waals) is due to the perturbation of the emitting atoms by other neutral atoms [42,43]. The FWHM is given by

$$\Delta\lambda^{V}_{1/2,L} = \frac{8.16}{2\pi\,c}\left(\frac{C_6}{\hbar}\right)^{2/5}\sqrt{\frac{8\,k_B\,T}{\pi\,\mu}}^{3/5}\,[X_0]\,{\lambda_{ki}}^2 \tag{36}$$

  The value of the broadening constant C_6 depends on the electronic polarizability of the perturbing atom and on the atomic radii of the emitter and the perturbing atom (see [44] for details). For this Lorentzian broadening, an approximation of the FWHM dealing with O, N, O_2 and N_2 at low temperature and low pressure is [40]

$$\Delta\lambda^{V}_{1/2,L}[\text{nm}] \approx T[\text{K}]^{-0,7}\,\frac{p[\text{Pa}]}{10^5} \tag{37}$$

- The pressure broadening due to the charged particles results from the static and dynamic electric fields they produce in the vicinity of the emitting atom or ion. This is therefore a Stark broadening. The theory developed to explain its main features requires to solve the Schrödinger equation taking into account the entire atomic structure of the emitting particle perturbed by Coulombic interactions due to the presence of many charged neighbors. If analytical solutions are known for the hydrogen atom, only approximated solutions can be derived for hydrogenlike or non-hydrogenlike cases. Each case results from the superposition of two limiting situations. The first situation deals with the impact approximation where the interaction duration is negligible with respect to the mean time between two successive collisions (case of the electrons). The second situation occurs for the opposite case where the perturbing particles can be considered as fixed (case of the ions). Then, they produce a quasi static electric field during the emission. This field has been described by Holtsmark [39,45]. Griem [43] contributed greatly to theorizing this approach and proposes approximations for isolated transitions without overlapping. The Stark broadening is of the Lorentzian type whose FWHM depends on electron density n_e and temperature T such as

$$\Delta\lambda^{S}_{1/2,L}(n_e,T) = 2\omega_{ki}(T)\,\frac{n_e}{n_{e,r}}\,\left[1 + 1.75\,\beta(n_e,T)\right] \tag{38}$$

  where $n_{e,r}$ is a reference value for n_e, ω_{ki} is the electronic impact factor and $\beta(n_e,T)$ is the following function

$$\beta(n_e,T) = A_S(T)\left(\frac{n_e}{n_{e,r}}\right)^{-\frac{3}{4}}\left[1 - \frac{3}{4}{N_D}^{-\frac{1}{3}}\right] \tag{39}$$

  where

$$N_D = 1.72\times 10^9\,\frac{T[\text{eV}]^{3/2}}{n_e[\text{cm}^{-3}]^{1/2}} \tag{40}$$

  is the number of particles in the Debye sphere.
  The values of ω_{ki} and A_S are tabulated as a function of temperature for reference electron densities $n_{e,r}$ for several transitions of different elements. The following default correlations are proposed by Fantoni et al. [46]

$$\omega_{ki}(T) = 4.8767\times 10^{-4} + 1.6385\times 10^{-8}T - 1.8473\times 10^{-13}T^2 \tag{41}$$

$$A_S(T) = 0.03983 - 7.0226\times 10^{-7}T + 9.5699\times 10^{-12}T^2 \tag{42}$$

  They can be reasonably used for $(10^{21} \lesssim n_e \lesssim 10^{25})$ m^{-3} and $(5{\times}10^3 \lesssim T \lesssim 3.5{\times}10^4)$ K [47]. Deviations from Griem values [43] can be significant, particularly for elements with low atomic numbers. Actually, these polynomial correlations are particularly appropriate to atoms and ions with a dense electronic structures like metals. As a result, these default correlations are used only if no bibliographic data is available.
  In the context of electron densities greater than some 10^{21} m^{-3}, the ionic contribution governed by the term $A_S(T)$ can be neglected. The following simplified expression can then be used

$$\Delta\lambda^{S}_{1/2,L}(n_e,T) = 2\,\omega_{ki}(T)\left(\frac{n_e}{n_{e,r}}\right) \tag{43}$$

Fig. 6 illustrates the evolution with n_e of the FWHM of most of the broadening types listed above for the monatomic mixture (O, O^+, e^-) at $T = 2\times 10^4$ K. The transition of interest chosen for this illustration is the O I triplet observed at 777.3 nm. The entrance slit width is 200 µm, which induces in our case to an apparatus function with a FWHM of $\Delta\lambda^{A}_{1/2,L} = 1.44\times 10^{-2}$ nm. We compare the Stark broadening obtained using the Griem values [43] (in green) with that resulting from the default correlation (Eq. (41), in purple). For the present case of oxygen, discrepancies between approximately 50% to 70% are observed for the n_e range considered. This means that the Stark effect is underestimated using the default correlation for this oxygen transition. Moreover, we notice that the Stark effect mainly drives the Voigt profile for $n_e \gtrsim 5\times 10^{22}$ m^{-3} for this value of T. For laser-induced plasmas, the concerned values of (T, n_e) induce the predominance of the Stark effect. Finally, Fig. 6 indicates that MERLIN can be reasonably simplified by considering only the broadening due to the apparatus function, to the Doppler effect (Eq. (34)), to the Van Der Waals interactions (Eq. (37)) and to the Stark effect (Eq. (38), (44)).

2.2.6. Spectral shift

The Stark effect can also lead to a spectral shift of the line whose influence on the calculated spectra can be significant. This spectral

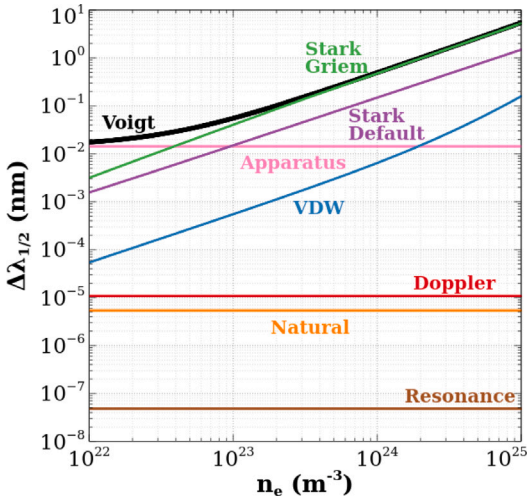

Fig. 6. FWHM of O I 777.3 nm for a monatomic mixture (O, O^+, e^-) at LTE ($T = 2 \times 10^4$ K) as a function of n_e. The Stark contribution becomes predominant for $n_e \gtrsim 5 \times 10^{22}$ m^{-3}.

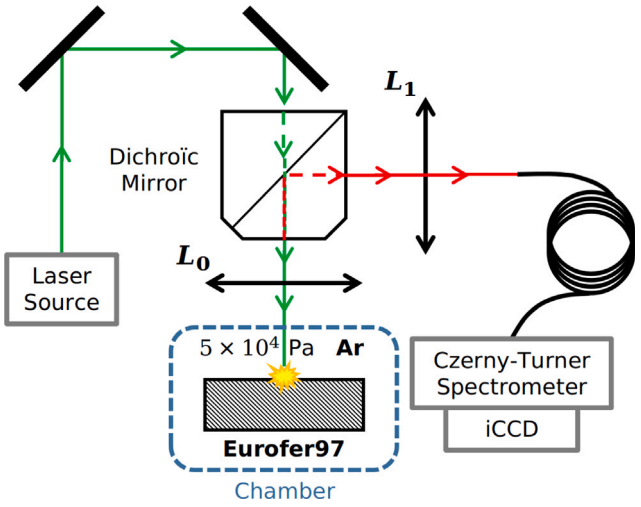

Fig. 7. Schematic view of the experimental validation device. The infrared laser pulse is transmitted by a dichroic plate then focused on the Eurofer97 sample (green optical path) placed in a controlled atmosphere chamber (5×10^4 Pa of Ar). The laser-induced plasma emission is retro collected collinearly in the direction of a fibered device (red optical path) connected to a spectrometer and a camera.

shift $\delta_{\lambda_{ki}}$ occurs towards higher or lower wavelengths depending on the species and the transition with

$$\delta_{\lambda_{ki}} = \omega_{ki}(T)\left[1.4 + 2A_S(T)\left(\frac{n_e}{n_{e,r}}\right)^{\frac{1}{4}}\left(1 - \frac{3}{4}{N_D}^{-\frac{1}{3}}\right)\right] \tag{44}$$

2.2.7. Influence of the data precision or database on the expected results

It is difficult in absolute terms to estimate the influence of a particular data or database on the expected results concerning the spectrum calculation. Indeed, the application of the radiative transfer equation (for instance under the form of Eq. (22)) leads to variable results, this equation being nonlinear with respect to the fundamental data. However, for the optically thin transitions that are predominant in the spectrum if the laser-induced plasma is observed at sufficiently late times, conclusions can be drawn. In this case, Eq. (23) drives the spectral radiance which is proportional to the emission coefficient. The precision of the data or the chosen database influences the results owing to Eqs. (24) to (43). Most cases correspond to a linear dependence.

3. Validation

3.1. Experimental aspects

The experiments are performed on the PLEIADES (Plasmas by LasEr IrrADiations and their Experimental Studies) platform of the CORIA laboratory [12]. The experimental setup is schematized in Fig. 7. Technical characteristics are listed on Table 1.

A nanosecond Nd:YAG QUANTEL Briant B laser source is used. The infrared laser pulse is reflected on three high flux mirrors (spectral reflectivity at 1064 nm $\tau_{1064} > 0.99$) in the direction of a high pass dichroic plate ($\tau_{1064} > 0.98$) and is then focused by the lens L_0 ($\tau_{1064} \sim 0.93$) positioned at 97 ± 1 mm from the surface of the sample. Under our operating conditions, the diameter of the laser spot on the sample surface is estimated to (275 ± 40) µm. This results in a peak fluence of (160 ± 50) J cm^{-2} which corresponds to a peak flux density of $(2.5 \pm 0.7) \times 10^{14}$ W m^{-2}.

The dichroic plate is characterized by a spectral reflectivity ρ_λ between 270 nm and 720 nm such that $0.20 < \rho_\lambda < 0.98$. The light emitted by the laser-induced plasma is therefore in part reflected by the plate towards a second lens L_1 which focuses the light collected on the entrance of a circular bundle of 19 optical fibers (Ø 200 µm, numerical aperture 0.22). The exit of these fibers are aligned on the entrance slit of a Teledyne SCT-320 spectrometer equipped with different gratings and cameras according to the spectral range of interest. The focal length of L_1 is chosen to maximize the collection of light owing to the fiber numerical aperture.

The acquisition is synchronized with each laser shot. The information travel time in the cables has been estimated to (72.5 ± 2.5) ns. As a result, two distinguishable times are separated by 2.5 ns. The acquisition time windows are all fixed at 50 ns to obtain a satisfactory temporal discretization owing to the plasma dynamics. Finally, each spectrum results from an accumulation of 10 laser shots within the same crater. The repeatability of the spectral emission of the plasma from one shot to another is ensured by the fact that the ablated depth is negligible compared to the ablation diameter [48] .

The apparatus function characterization is carried out using a low pressure Hg lamp. The protocol for collecting radiation from this lamp is strictly the same as the one adopted for the study of laser-induced plasma. The measurement of the FWHM of the Hg I 275.28 nm line as a function of the spectrometer slit aperture width for the grating at 3600 g mm^{-1} is shown in Fig. 8. The emission of this type of lamp does not present any physical broadening experimentally measurable with our device. Thus, the observed FWHM strictly corresponds to the apparatus function of our acquisition equipment. We notice that our collection system is similar to a double diaphragm. Indeed, at a low opening value of the slit, the collected signal is diaphragmed by the entrance slit of the spectrometer whereas at a high aperture value it is the bundle of optical fibers which diaphragms the incident radiation. This is characterized by the fact that the measured FWHM no longer changes for $f_e > 200$ µm, which corresponds to the diameter of a fiber of the bundle used for the collection of radiation. The purely Lorentzian nature of the apparatus function is highlighted by the interpolation illustrated on the bottom of Fig. 8.

The spectra presented in this paper are all calibrated in spectral radiance. The calibration for $\lambda < 400$ nm is carried out using an H_2D_2 arc lamp using a stabilized power supply. For $\lambda > 400$ nm, we use a W ribbon lamp whose radiance temperature is known as a function of the power injected into the ribbon. The collection of radiation from these two devices is carried out exactly in the same way as the collection of radiation from laser-induced plasma. In addition, the wavelength calibration is obtained by using low pressure rare gas lamps.

Table 1
Technical characteristics associated to Fig. 7 device.

Optical element	Data	Symbol	Value
QUANTEL Briant B laser source	Pulse wavelength	λ_L	1064 nm
	Energy	E_L	45 mJ
	Pulse duration	τ_L	6.0 ns
	Repetition rate	ν	10 Hz
	Quality factor	M^2	3.0
	Pulse-to-pulse stability	$\Delta E_L/E_L$	0.1%
L_0	Focal length	f_0	100 mm
L_1		f_1	40 mm
Princeton Instruments	Focal length	f_s	320 mm
SCT-320 spectrometer	Aperture	$f_s/4.6$	
	Grating	G	600 g mm^{-1} & 3600 g mm^{-1}
	Optical fiber diameter	d_s	200 µm
PI-MAX 4 VUV camera (1024 × 1024 pixels)	Pixel size		13 × 13 µm^2
	Quantum efficiency at 274 nm	η	13%
PI-MAX 4 HBf camera (1024 × 1024 pixels)	Pixel size		13 × 13 µm^2
	Quantum efficiency at 650 nm	η	37%

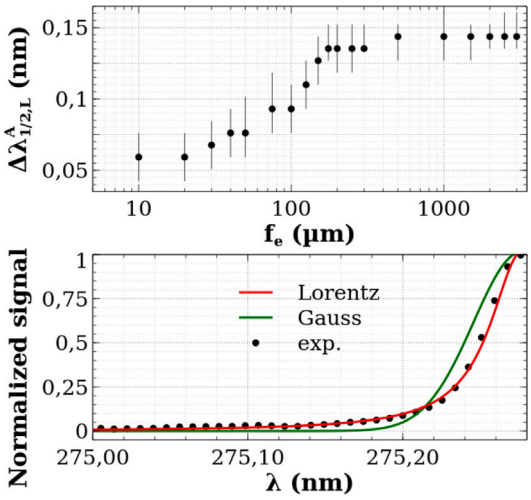

Fig. 8. Top: FWHM of the Hg I 275.28 nm line as a function of the entrance slit width of the spectrometer. Bottom: normalized reconstructions of the spectral half-profile of the Hg I 275.28 nm line for $f_e = 10$ µm.

Table 2
Mole fractions (precision of 10^{-4}) of the EF97 sample studied. The reference composition is obtained by X-ray fluorescence (XRF subscript) [50]. The LIBS composition resulting from our study does not take into account elements whose mole fraction is < 500 ppm.

Element	$x_{X,XRF}$	$x^*_{X,LIBS}$
Fe	0.8530	0.8907
Cr	0.0977	0.0626
Cu	0.0222	0.0216
W	0.0035	0.0034
Na	0.0147	0.0143
Mn	0.0055	0.0053
V	0.0021	0.0021
Se	< 0.0004	–
Co	< 0.0003	–
K	< 0.0003	–
Zn	< 0.0002	–

3.2. Sample and background atmosphere

The sample selected for this experimental validation campaign is a Eurofer97 (EF97) steel sample. This material is used for the vacuum chambers of thermonuclear fusion reactors. The sample we have is sufficiently homogeneous to guarantee the absence of composition gradients and to ensure the repeatability of the emission from one laser shot to the other [13]. The surface is polished prior to the measurement campaign in order to obtain an average roughness of (58.5 ± 2) µm. This steel is mainly composed of Fe, Cr and Cu (see Table 2). The choice of a ferric alloy is motivated by the presence of several Fe II transitions observable in the near ultraviolet without the need to implement a device adapted to spectroscopic study below 180 nm [49]. For our LIBS study, we have neglected the elements with a mole fraction lower than 500 ppm. This affects, at the margin, the value of the concentration of minor elements which are not spectrally studied. Considering the composition obtained by X-ray fluorescence as a reference, we note a difference of 4.42% for Fe, 56.07% for Cr and 2.78% for Cu with those obtained from LIBS spectroscopic analysis (detailed in the following). These discrepancies are mainly explained (1) by the uncertainties linked to the estimate of the experimental spectral baseline, (2) by the calibration in spectral radiance and (3) by the lack of spectroscopic data (in particular for Cr II). These different aspects are detailed below.

Considering the LIBS composition of Table 2, we can quantitatively discuss the composition of species in the plasma as a function of temperature at fixed pressure. We present in Fig. 9 the composition of an EF97 plasma over a wide range of temperatures at $p = 5 \times 10^4$ Pa. With the exception of Na, the ionization potentials of all the elements of the mixture are similar (ranging from 6 eV to 8 eV). The evolution with temperature of the degree of ionization of each element is therefore similar from one species to the other. Our measurements show, more particularly at the first moments of the dynamics, that considering a double ionization is necessary to correctly characterize the physico-chemistry of the plasma. Indeed, for most of the elements X, at $T \sim 1.5\times10^4$ K, we notice that $n_{X^+} \sim 10\, n_{X^{2+}}$. Although at lower temperature $n_{X^{2+}}$ can be neglected, all modeling results presented in the paper have been obtained including a double ionization.

The experiments presented below have been carried out under argon with purity > 99.999% at a pressure of $(5.0 \pm 0.2) \times 10^4$ Pa in order to ensure the homogeneity of the laser-induced plasma [49]. A procedure based on successive pumpings and argon fillings of the analysis chamber is performed before the acquisitions. Most of the residual impurities present in the chamber are then evacuated. We use polymer pipes (polyamide 11) for the injection of argon into the chamber. This induces the presence of hydrogen leading to the possibility of a precise measurement of the electron density based on the Balmer H_α line. The presence of argon in which the laser-induced plasma expands rapidly leads to a high mole fraction for argon in the plasma: argon is then the main element, the metallic elements from the EF97 alloy being rather weak. In our case, the summation of the mole fractions of these elements in the plasma is equal to the factor

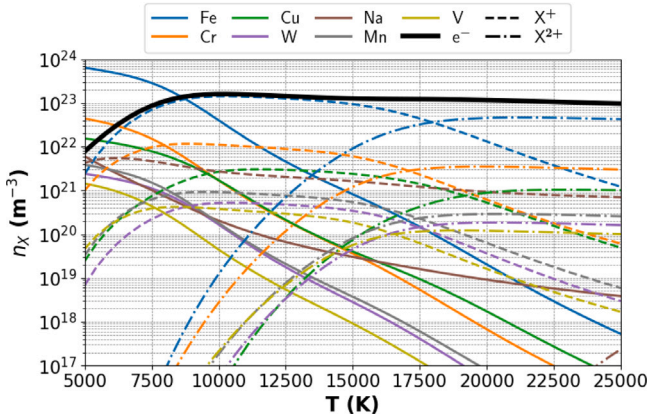

Fig. 9. Evolution with temperature T of the LTE composition of an EF97 plasma ($x^*_{X,LIBS}$, Table 2) at $p = 5 \times 10^4$ Pa. The color indicates the species. The type of line gives the ionization state. Electron density is shown as a thick solid black line.

$$\zeta = 1 - (x_{Ar} + x_H) \tag{45}$$

Thus, the mole fraction of the element X within the sample is

$$x^*_{X,LIBS} = \frac{x_{X,LIBS}}{\zeta} \tag{46}$$

3.3. Plasma size measurement

In the case of a homogeneous plasma, the calculation of the radiative transfer requires the thickness of the emitting plasma (Eq. (22)). The fiber assembly described in Section 3.1 does not allow plasma imaging. An additional setup allowing the observation of the plasma tangentially to the surface irradiated by the laser pulses has been implemented. This standard setup consists in two converging lenses with focal lengths of 150 mm and 500 mm (magnification 3.33) and an absorbent density protecting the photodetector of a PI-MAX 4 HRf camera. The number of shots in the same crater is adapted to maintain a satisfactory signal level. The signal level of the images obtained is reduced to a single laser shot and normalized over the entire plasma dynamic. We then obtain images such as those in Fig. 10.

We then spatially integrate the signal over the entire height of the sensor in order to obtain an emission profile. The measurements of the FWHM ($y_{\ell_1} = 0.5$) of this profile are used to obtain the values displayed on Fig. 11. The uncertainties on the abscissa correspond to the acquisition time of the camera. The uncertainties on the ordinate correspond to the plasma dimension values respectively associated with $y_{\ell_1} - 0.1$ and $y_{\ell_1} + 0.1$. Since, to our knowledge, no paper provides an unanimously adopted criterion for the value of y_{ℓ_1}, we have considered a widened confidence interval. Considering $y_{\ell_1} = 1/e^2$ leads to higher values of ℓ_1 with an average deviation of around 32%. The reconstructions of the experimental spectra presented below are only slightly affected by this discrepancy.

The temporal dynamics of ℓ_1 displayed on Fig. 11 is interpolated by a power law of the type $\ell_{1,0}\left(\frac{t}{t_0}\right)^B$ with $B = 0.191$ and $\ell_{1,0} = 645$ µm for $t_0 = 10$ ns. Since t_0 is the order of magnitude of the absorption duration of the laser pulse, we can consider $\ell_{1,0}$ as the initial thickness of the plasma for the following dynamics. At the first times, the expansion speed resulting from the measurements of ℓ_1 is of the order of $\sim 2 \times 10^3$ m s^{-1}. At the last moments of measurement, this speed is estimated at $\sim 3 \times 10^2$ m s^{-1} (near the limit condition of sonic expansion).

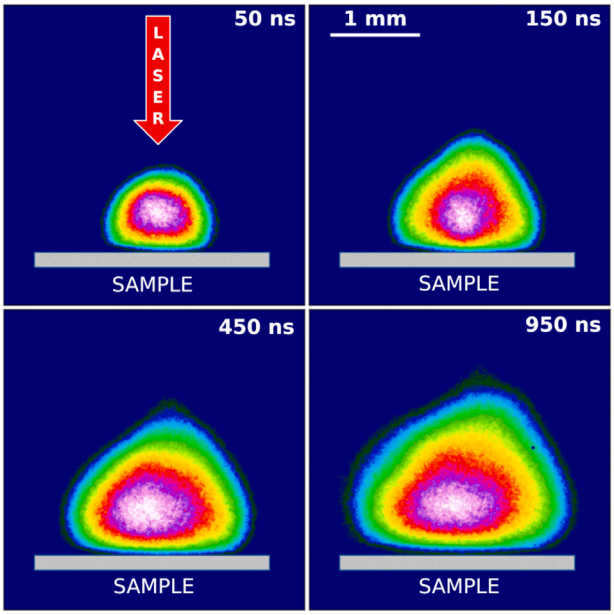

Fig. 10. Characteristic post-processed images of the Eurofer97 laser-induced plasma in argon atmosphere acquired perpendicularly to the laser optical axis at times $t = 50$ ns, $t = 150$ ns, $t = 450$ ns and $t = 950$ ns.

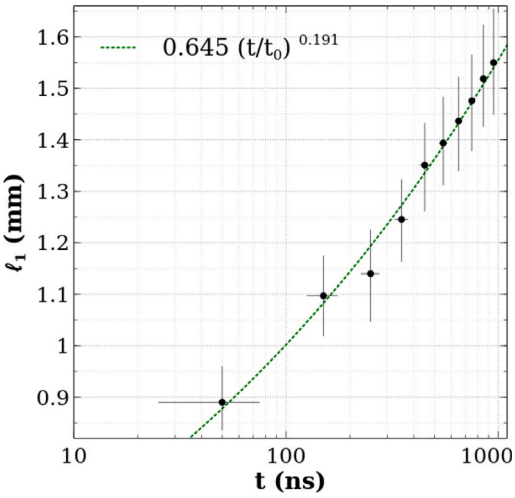

Fig. 11. Temporal evolution of the height (total FWHM of the profile resulting from the images in Fig. 10) of the EF97 laser-induced plasma whose irradiation conditions are described in Section 3.1.

3.4. Electron density measurement

As stated in Section 2, calculating the population densities of the emitting levels requires knowing (T, p) or (T, n_e) in addition to the elemental composition of plasma. In the case of laser-induced plasmas, it is difficult to perform a direct measurement of the plasma pressure p. Thus, we measure n_e by exploiting the Stark broadening and shift of judiciously selected transitions. We preferentially choose transitions of the main element in the plasma, i.e. argon. We have analyzed Ar II transitions (sensitive to high densities) as well as Ar I transitions for the last moments of the recombination phase. All of these transitions have the advantage of being spectrally isolated, well described in the literature and characterized by a measurable Stark shift. These measurements are coupled to the analysis of the H I line at 656.28 nm which is frequently used due to its high sensitivity to electron density. The apparatus function being Lorentzian and the Lorentzian contribution

Table 3
Ar and H transitions studied for the measurement of n_e. Stark impact factors ω_{ki} are given for a reference perturber density $n_{e,r} = 10^{22}$ m^{-3}. Stark shift factors δ_{ki} are given for reference perturber density $n_{e,r} = 10^{22}$ m^{-3} for $T \in [10^4, 2.65 \times 10^4]$ K.

Element	λ_{ki} (nm)	A_{ki} (10^7 s^{-1})	E_i (eV)	E_k (eV)	g_i	g_k	ω_{ki} (pm)	δ_{ki} (pm)	Ref.
Ar II	648.31	1.06	18.061	19.972	4	2	6.52	1.67	[24,51]
H I	656.28	6.46	10.199	12.087	4	6	106.56	5.14	[24,52,53]
Ar II	664.37	1.47	17.629	19.494	10	8	7.18		[24,51]
Ar II	668.43	1.07	17.695	19.549	8	6	6.16	0.57	[24,51]
Ar II	675.65	0.20	17.776	19.610	4	4	6.28	0.96	[24,51]
Ar II	686.35	0.25	17.734	19.549	6	6	5.54	0.48	[24,51]
Ar II	688.66	0.09	17.695	19.494	8	8	6.59	0.58	[24,51]
Ar I	696.54	0.64	11.548	13.328	5	3	6.67	3.03	[24,51]
Ar I	706.72	0.38	11.548	13.302	5	5	6.60	2.73	[24,51]
Ar I	714.70	0.06	11.548	13.283	5	3	6.33	3.30	[24,51]

to the Stark effect being predominant, we can reasonably consider that the line profile is purely Lorentzian. This greatly simplifies the deconvolution operation between the apparatus function and the Stark contributions. The transitions studied as well as the Stark data used for the n_e measurement are listed in Table 3.

The self-absorption correction factor C_{ki}^{SA} is defined as the ratio between the radiance L_{ki} of the self-absorbed transition and the radiance L_{ki}^{OT} of this same transition $k \to i$ considered optically thin. As explained in Section 2.2, a transition can be considered optically thin if $\alpha_\lambda \ell_1$ is sufficiently weak to allow a Taylor expansion of the spectral transmittivity of the plasma $\exp(-\alpha_\lambda \ell_1)$. This results in a self-absorption correction coefficient defined by

$$C_{ki}^{SA} = \frac{L_{ki}}{L_{ki}^{OT}} = \frac{\int_{-\infty}^{+\infty}(1 - e^{-\alpha_\lambda \ell_1})\,\mathrm{d}\lambda}{\int_{-\infty}^{+\infty} \alpha_\lambda \ell_1\,\mathrm{d}\lambda} \tag{47}$$

The n_e value of a laser-induced plasma is large enough to consider the profile as purely Lorentzian due to the contribution of the Stark effect. We therefore obtain the approximation

$$C_{ki}^{SA} \approx \left[\frac{\Delta\lambda^{SA}}{2\omega_{ki}} \frac{n_{e,r}}{n_e}\right]^{\frac{b}{a}} \tag{48}$$

where the coefficients $a = -0.54$ and $b = 0.46$ are given by El Sherbini et al. [54]. The high concentration of argon can lead to self-absorption and a bias in the broadening measurement. This is why the measured electron density is corrected by taking into account the line self-absorption. Since C_{ki}^{SA} depends on n_e, an iterative procedure is implemented to converge, for each transition, to the measured value of the electron density. The final value of n_e is the average of those obtained by Stark broadening and shift measurements. This average is weighted by C_{ki}^{SA}, by the precision of the Stark data provided by [51–53] as well as by the measurement uncertainty. This leads to favor the least self-absorbed transitions as well as those whose Stark data and the usability of the experimental spectrum allow a more precise measurement. This procedure is repeated for each time along the plasma dynamics and leads to Fig. 12 results.

On this plot, the horizontal uncertainty bars correspond to the integration time of the signals. The vertical uncertainty bars correspond to the standard deviation of the statistics carried out for all the transitions used. We note a particularly large uncertainty at time $t = 50$ ns. This is linked to the fact that only the transitions Ar II 664.37 nm and Ar II 668.43 nm can be used to determine the electron density. Indeed at this time, the signal to baseline ratio is low and limits the precision of the broadening measurement. The standard deviation resulting from the statistics based on these two measurements is significant. We have therefore excluded this first value from the power law interpolation of the type $n_{e,0}\left(\frac{t}{t_0}\right)^B$ which satisfactorily matches the rest of the temporal evolution. The interpolation of all the other points of the dynamics is indeed satisfactory with $B = -1.105$, $t_0 = 10$ ns and $n_{e,0} = 2.33 \times 10^{25}$ m^{-3}. This value is compatible with the limiting condition of density of the solid ($< 10^{28}$ m^{-3}) owing to the expansion and consistent with measurements carried out elsewhere [55].

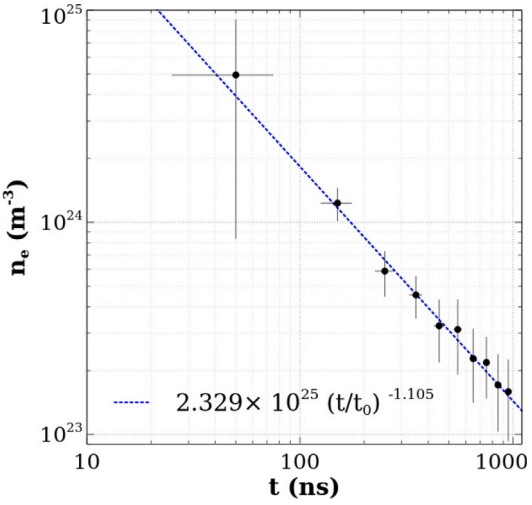

Fig. 12. Temporal evolution of the electron density of the EF97 laser-induced plasma whose irradiation conditions are described in Section 3.1.

3.5. Temperature measurement

The main assumption of the MERLIN code is the achievement of LTE. This assumption can be verified by considering the McWhirter criterion giving a minimum electron density at fixed electron temperature to obtain the equilibrium. For an argon plasma (surrounding gas) at $(10^4 < T < 1.5 \times 10^4)$ K, this electron density threshold varies between $2.46{\times}10^{23}$ m^{-3} and $3.02{\times}10^{23}$ m^{-3}. The major element of EF97 (Fe), due to its particularly dense electronic structure in energy levels, exhibits electron density thresholds of the order of 100 times lower than those of argon at the same temperatures. The measurements in Section 3.4 therefore reveal that LTE is systematically verified in our experimental conditions.

The linear trend of the points in a Saha–Boltzmann (SB) plot allows the precise verification of LTE and the determination of the plasma temperature. For the neutral transitions, the ordinate is obtained from an experimental measurement of the line radiance $L_{ki} = \int_{-\infty}^{+\infty} L_{\lambda,T}\,\mathrm{d}\lambda$ weighted by the ratio of spectroscopic data $\frac{\lambda_{ki}}{A_{ki} g_k}$. The points associated with neutral transitions are positioned on the abscissa according to their value of E_k. For the ionic lines, the procedure is the same except that we correct the ordinate by the factor $ln\left(\frac{2(2\pi m_e k_B T)^{3/2}}{n_e h^3}\right)$ and the abscissa is given by $E_k + E_{io}$ [56]. The value of n_e in the ordinate correction is experimentally known (see Section 3.4). The value of T in the ordinate correction is estimated by comparing the black body radiance with the one of the Fe II transitions located between 274.5 nm and 275 nm. Indeed, these transitions are strongly self-absorbed and the spectral radiance then leads to the one of the black body (see Eq. (22) with $\alpha_{\lambda_1} \to \infty$). As a result, those lines are not used for the temperature determination from the SB plot. This is not a limiting situation

Table 4
Fe transitions considered for the measurement of T [24].

Element	λ_{ki} (nm)	A_{ki} (10^7 s^{-1})	E_i (eV)	E_k (eV)	g_i	g_k
Fe II	292.66	0.51	0.986	5.221	8	10
Fe II	298.48	4.30	1.671	5.823	6	6
Fe II	300.26	1.79	1.695	5.823	4	6
Fe II	307.72	1.40	4.076	8.104	14	12
Fe II	315.42	2.06	3.768	7.697	10	10
Fe II	316.78	1.60	3.814	7.727	8	8
Fe I	322.58	11.80	2.399	6.242	11	13
Fe II	322.77	0.89	1.671	5.511	6	8
Fe I	354.11	8.65	2.851	6.351	9	11
Fe I	360.67	8.29	2.692	6.129	11	13
Fe I	376.55	9.51	3.237	6.528	13	15
Fe I	381.58	11.20	1.485	4.733	9	7
Fe I	382.04	6.67	0.859	4.103	11	9

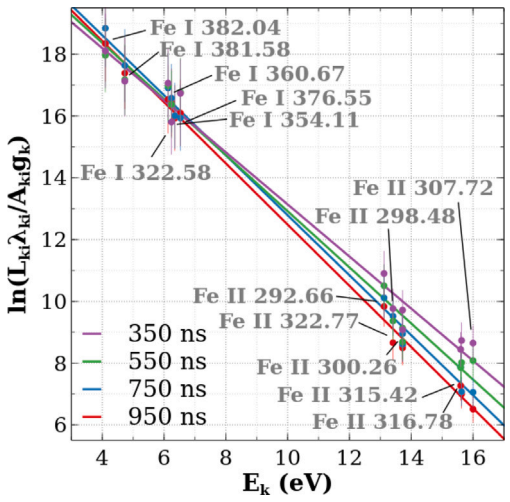

Fig. 13. Saha–Boltzmann diagrams obtained from the study of the transitions of the Table 4 at times $t = 350$ ns, $t = 550$ ns, $t = 750$ ns and $t = 950$ ns. The correction of the ordinates of the points associated with the Fe II transitions is carried out in accordance with the paper by Safi et al. [56].

because many other iron transitions are possible and the weakness of the Fe mole fraction in the plasma strongly reduces the possibility of self-absorption and consequently the bias on L_{ki}. Additionally, Fe is characterized by an electronic structure suitable for temperature measurements because many transitions can be observed whose upper level corresponds to excited energy E_k distributed over wide ranges.

The Fe I and Fe II transitions studied are listed in Table 4. The averaged uncertainty of the spontaneous emission probabilities is $< 5.7\%$ for Fe I and $< 27.2\%$ for Fe II [24]. Even if these uncertainties are significant, the most important source of uncertainty lies in the determination of L_{ki}. Indeed, although our calibrated signals are processed with a baseline subtraction module [57], the net signal very rarely presents a strictly zero baseline. This has the effect of overestimating the value of L_{ki}.

The Saha–Boltzmann plots are displayed on Fig. 13 for times $t = 350$, 550, 750 and 950 ns along the plasma dynamics. The T values involved in the ordinate correction of the Fe II points (comparison of the black body radiance and the Fe II lines emission ranging between 274.5 nm and 275 nm) are respectively (13140 ± 525) K, (12430 ± 350) K, (11650 ± 350) K and (11500 ± 350) K. The exploitation of the SB plots from the slope of the linear interpolation leads to the following temperature (13760 ± 525) K, (12770 ± 350) K, (11950 ± 350) K and (11710 ± 350) K. At these times, we therefore note a mean difference between the estimate of T via the black body on [274.5, 275] nm and the approach by SB plots of the order of 3%. This allows us to consider that the quality of our spectral radiance calibration is sufficient to

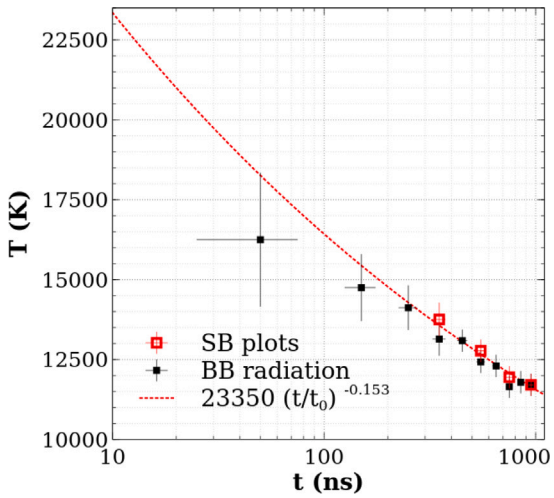

Fig. 14. Temporal evolution of the temperature of the EF97 laser-induced plasma whose irradiation conditions are described in Section 3.1. SB plots and BB radiance on [274.4, 275] nm measurements are respectively indicated by red open squares and black squares.

directly measure T from the black body radiance during the plasma dynamics.

On Fig. 14, the plasma temperatures obtained from the SB plots at times $t = 350, 550, 750$ and 950 ns (red open squares) and from the BB radiance on [274.4, 275] nm at times $t = 50$, 150, 250, 350, 450, 550, 650, 750, 850 and 950 ns (black squares) are simultaneously plotted. The horizontal uncertainty bars correspond to the integration time of the signal. The vertical uncertainty bars correspond to the temperature interval allowing a satisfactory reconstruction of the experimental spectrum on [274.4, 275] nm. We have noted that the uncertainty in the value of T is greater when the continuous contribution to the signal is strong. Similarly to n_e and ℓ_1, we have interpolated this evolution with a usual power law of the type $T_0 \left(\frac{t}{t_0}\right)^B$. Since (1) the continuous contribution to the signal does not allow a precise measurement of T at early times and (2) we have observed also at early times a lack of homogeneity of the plasma marked by absorption dips on the lines Ar I 696.54 nm and Ar I 706.72 nm due to cold edges, $t = 50$ and 150 ns have not been taken into account for the interpolation. The values $B = -0.153$ and $T_0 = 23350$ K have then been derived. Since t_0 corresponds to the characteristic time of the laser pulse absorption, $T_0 = 23350$ K can be considered as the initial temperature. This value is in very good agreement with similar measurements [55].

Knowing L_{ki}, we can experimentally estimate the ratio $[X_k]/g_k$ by the relation

$$\frac{[X_k]}{g_k} = \frac{4\pi}{hc}\frac{\lambda_{ki}}{A_{ki}g_k}\frac{L_{ki}}{\ell_1} \tag{49}$$

if the transition is optically thin. For each line, the experimental measurement of the population density per quantum state of the emitting level can then be compared to the value obtained by the calculation using Eq. (30) assuming known the plasma composition, n_e and T. This comparison is illustrated by Fig. 15 at times $t = 350$, 550, 750 and 950 ns. The averaged deviation of the experimental points from the linear trends of the calculation is $< 50\%$. The mean deviation between the temperatures obtained from neutral transitions (in blue) and ionic transitions (in red) is of the order of 12%. We also notice that the linear trend for the neutrals as for the ions is further marked at later times in the plasma dynamics. This is explained by the fact that the exploitation of the experimental data is more reliable when the electron density is low (negligible contribution from continuous emission and low line overlapping).

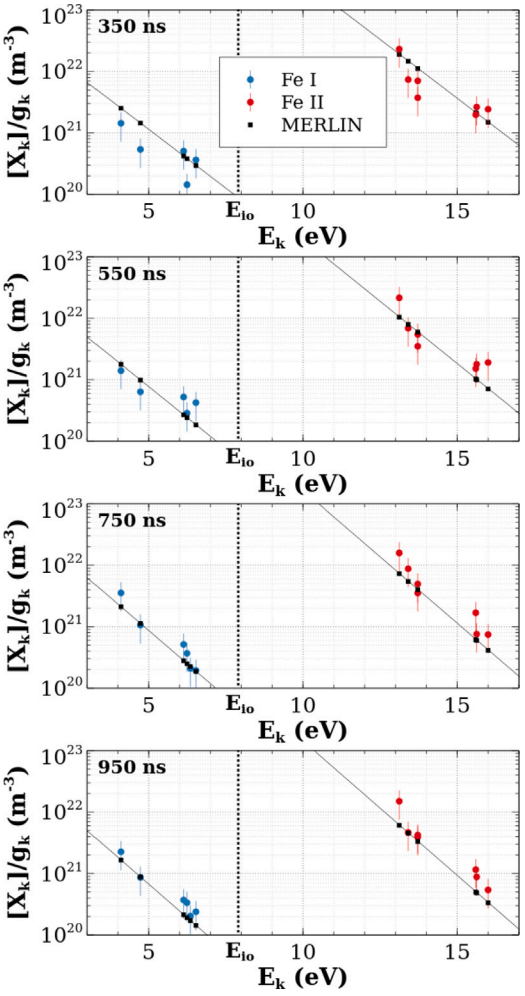

Fig. 15. Population densities per quantum state of the emitting levels of the transitions listed in Table 4 weighted by their degeneracy at times $t = 350$ ns, $t = 550$ ns, $t = 750$ns and $t = 950$ ns. The experimental points of Fe I and Fe II are shown in blue and red, respectively. The LTE calculation values are indicated in black.

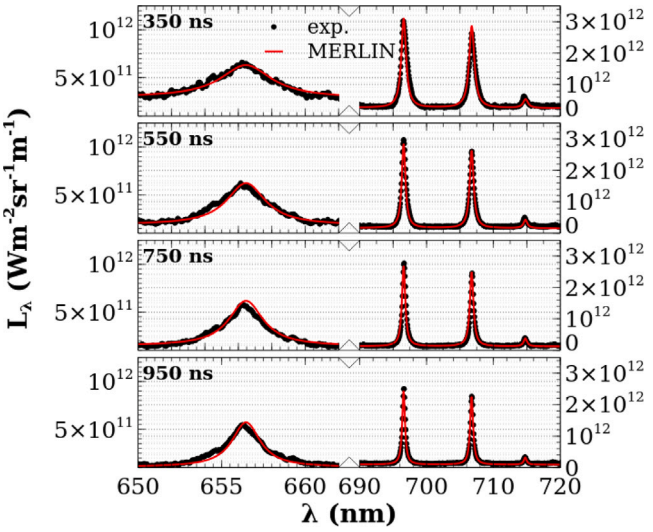

Fig. 16. Comparison of experimental spectra (in black) and simulated spectra (in red) over the spectral interval [650, 720] nm at times $t = 350, 550, 750$ and 950 ns.

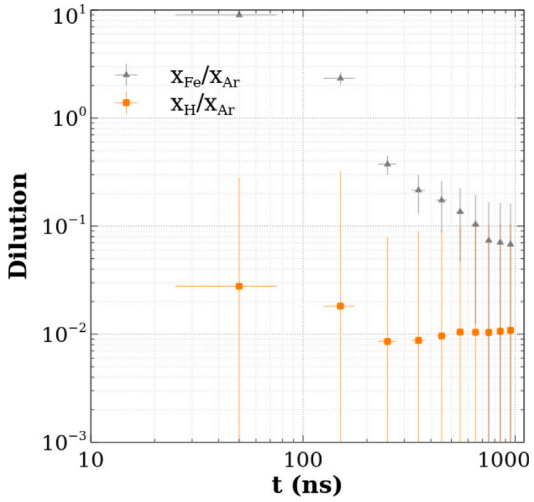

Fig. 17. Temporal evolution of the ratios x_{Fe}/x_{Ar} (in gray) and x_H/x_{Ar} (in orange) measured for the EF97 laser-induced plasma whose irradiation conditions are described in Section 3.1.

3.6. Plasma dilution dynamics

Here we focus our attention on the emission of argon and hydrogen during the plasma dynamics. Since $x^*_{X,LIBS}$ (Table 2), ℓ_1 (Fig. 11), n_e (Fig. 12) and T (Fig. 14) have been determined, the plasma dilution can be studied through the mole fractions x_{Ar} and x_H (Eqs. (45) and (46)). The simulation of the experimental spectra at times $t = 350, 550, 750$ and 950 ns have been performed using MERLIN and is displayed on Fig. 16. The [662, 690] nm interval has been intentionally excluded from the calculation because this range involves many metallic lines (notably Fe I, Cr I and W I), the broadening parameters of which are not available in the literature.

The Ar I 696.54 nm, Ar I 706.72 nm and Ar I 714.70 nm transitions allows the determination of x_{Ar}. For $t < 250$ ns, it is difficult to clearly distinguish the emission of the H I 656.28 nm line from the continuous emission owing to its strong Stark broadening. For later times, the line is observable. From the mole fractions x_{Ar} and x_H then obtained, we have calculated the ratios x_{Fe}/x_{Ar} and x_H/x_{Ar} representative of the dilution process by the background gas. Their time evolution is illustrated by Fig. 17. The horizontal uncertainty bars correspond to the temporal integration range of the signal. The vertical uncertainty bars are obtained from the uncertainties in x_{Fe}, x_{Ar} and x_H. The uncertainty in the Fe mole fraction is determined from the difference in $x_{Fe,XRF}$ (considered as a reference) and $x_{Fe,LIBS}$. The uncertainties on the Ar and H mole fractions are determined from the MERLIN calculations and are of the order of 10% depending on the time considered. From the values of x_H and considering that argon coming from the seeding bottle contains a negligibly small quantity of hydrogen, we estimated the averaged degassing rate of the internal walls of our device at $\sim 3 \times 10^{14}$ s^{-1} cm^{-2} $\approx 10^{-5}$ Torr l s^{-1} cm^{-2} during the acquisitions. This value is in agreement with measurements on polymers [58] and consistent with information relating to the degassing of steels [59]. On the other hand, the non-homogeneity of the plasma observed at times $t = 50$ and 150 ns does not allow a clear decision on the dilution, which generates an increase in uncertainties at these two times. The dynamics shows that the plasma is mainly metallic in the first $\approx$ 200 ns of its dynamics, a strong dilution then occurs leading to a negligible amount of Fe compared to argon at $t \approx 600$ns.

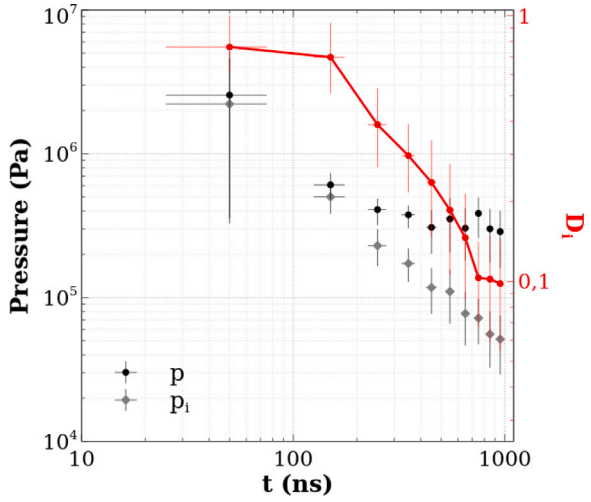

Fig. 18. Temporal evolutions of kinetic pressures (obtained by the LTE calculation carried out from our measurements of $(n_e, T, x_{Ar}, x_H) = f(t)$, in black) and charge pressure (obtained from Eq. (51) and our measurements of $(n_e, T) = f(t)$, in gray) of the EF97 laser-induced plasma whose irradiation conditions are described in Section 3.1. The dynamics of the ionization degree D_i is indicated in red.

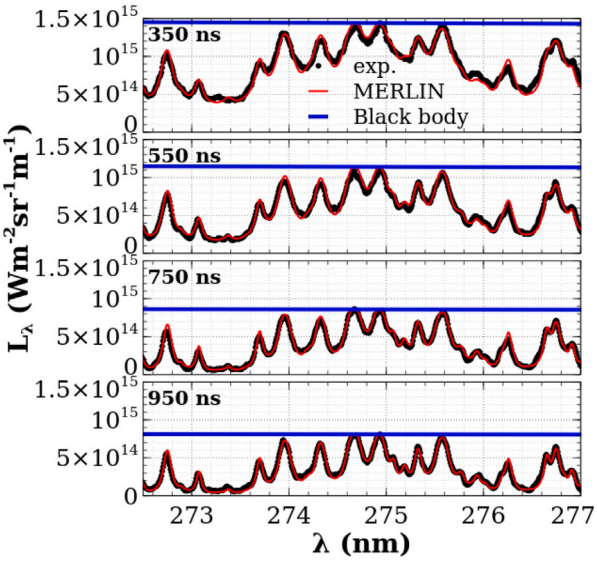

Fig. 19. Comparison of experimental spectra (in black) and simulated spectra (in red) over the spectral interval [272.5, 277] nm at times $t = 350, 550, 750$ and 950 ns. The black body spectral radiance is plotted in blue.

3.7. Recombination analysis

We can further analyze the global coherence between the results presented above. The $n_e(t)$ and $T(t)$ evolutions finally lead to

$$n_e(T) = n_{e,0}\left(\frac{T}{T_0}\right)^{7.222} \tag{50}$$

From (T, n_e), the pressure

$$p_i = 2n_e k_B T \tag{51}$$

due to the charged particles can be derived if the singly charged ions are predominant. From the composition, the total pressure

$$p = \sum_X n_X k_B T \tag{52}$$

of the plasma can also be deduced. From the densities $n_{X\ I}$ of the neutral species of the plasma, its ionization degree D_i is therefore

$$D_i = \frac{n_e}{n_e + \sum_X n_{X\ I}} \tag{53}$$

The time evolution of p_i, p and D_i is illustrated by Fig. 18. The horizontal uncertainty bars correspond to the integration time of the signal. The vertical uncertainty bars are obtained from the uncertainties in n_e, T and (x_{Ar}, x_H). We see that the boundary condition $p \approx p_i$ when $D \sim 1$ is satisfied, since the main ions are singly charged. As recombination occurs, the ionization degree decreases and the plasma pressure is no longer controlled by ions. The decoupling between p and p_i takes place around $(200 < t < 300)$ ns when $0.4 < D_i < 0.7$. On the other hand, we note that $p(t = 950\ \text{ns}) > 1.013 \times 10^5$ Pa. This value is consistent with the plasma expansion speed value observed in Section 3.3.

3.8. Simulation of the emission around 274.5 nm

All of the developments presented in Sections 3.1, 3.3, 3.4, 3.5 and 3.6 lead to the reconstructions of Fig. 19.

These simulations are based on a LTE plasma composed with the main 9 elements Ar, H, Fe, Cr, Cu, W, Na, Mn, V of EF97 (see Table 2). Then 28 species are included: the previous elements under neutral, singly and doubly ionized states and e^-. Simulating the experimental emission over the interval [272.5, 277] nm has required the contribution of 770 transitions. In the present situation the Stark effect is the main cause to the line broadening. The spectral and Stark data are the only parameters controlling the fidelity of the reconstruction. Some of them are missing. To overcome this difficulty, information from NIST database [24] has been prioritized and the default polynomial correlation for the Stark impact factor ω_{ki} (Eq. (41)) and a Stark shift $\delta_{ki} = 0$ have been considered. Table 5 summarizes the sources used.

Table 5
Sources of spectral and Stark data used for simulating the emission of the [272.5, 277] nm spectral range. For any unlisted plasma species: **Ref.** Spectral: [24] and **Ref.** Stark: [46].

Element	Ref. Spectral	Ref. Stark
Fe I	[24,60]	[55]
Fe II	[24,60]	[55]
Fe III	[60]	[46]
Cr II	[60]	[55]
Cu II	[61]	[46]
W I	[38]	[46]
W II	[38]	[46]
W III	[38]	[46]
Mn II	[60]	[46]
Mn III	[60]	[46]
Na II	[61]	[46]
Na III	[61]	[46]
V II	[60]	[46]
V III	[60]	[46]
H I	[24]	[52,53]

The degree of fidelity of the simulation increases with time t. This can be justified from the following factors:

- due to the simplification of Section 2.2.2 concerning radiative recombination and thermal Bremsstrahlung, the continuum is underestimated.
- the continuum is assumed to only depend on the argon number density. As put forward by the dilution process analyzed in Section 3.6, the mole fraction in argon increases with time and a few moments after its formation, the plasma mainly contains iron. Nevertheless, the impact of this assumption should be put into perspective given the small relative differences in the continuum contributions of Ar and Fe plasmas [62].

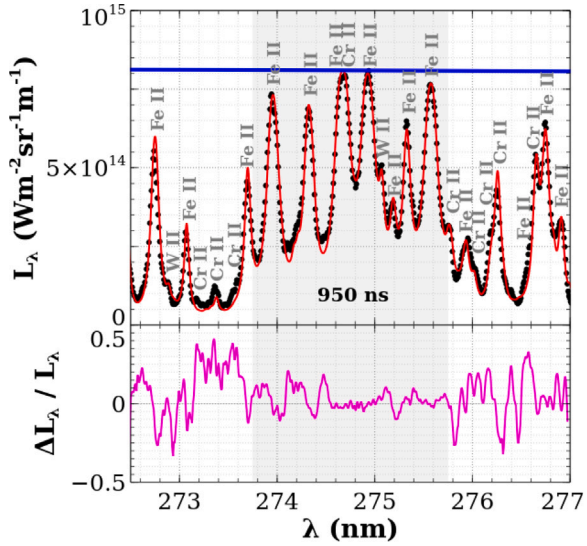

Fig. 20. Detailed comparison of the experimental spectrum at time 950 ns (in black) with its simulation (in red) for $(n_e, T, \ell_1, x_{Ar}, x_H) = (1.8 \times 10^{23}\ \mathrm{m}^{-3}$, 11 500 K, 1540 µm, 0.92, 0.01) on [272.5, 277] nm. The black body spectral radiance at T = 11 500 K is shown in blue. At the top: the spectrum, at the bottom: the relative difference in spectral radiance.

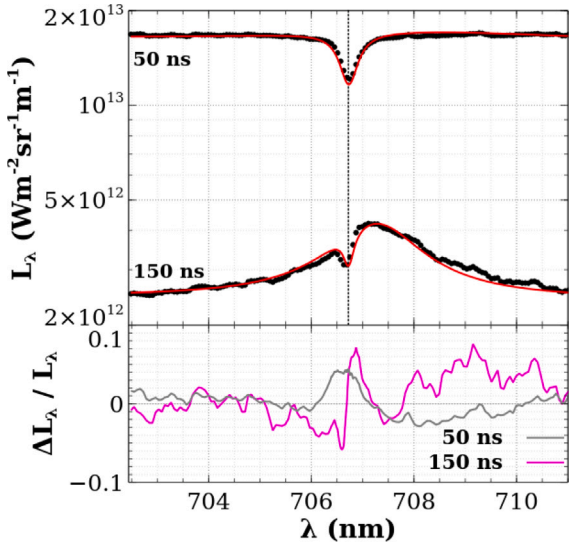

Fig. 21. Top: experimental spectra at times t = 50 and 150 ns (in black) and spectra calculated with MERLIN (in red) on the [702.44, 711.00] nm spectral range. The central plasma is characterized by $(n_e, T, \ell_1, x_{Ar}, x_H)$ previously determined. The thickness of the cold layer is fixed at $\ell_2(t) = 0.1\ell_1(t)$ with the same composition as in the central plasma. The computation is obtained by optimizing the couple (T_2, n_{e_2}). Bottom: relative difference in spectral radiance.

- the T dependence of ω_{ki} is rarely reported in literature. The available information is generally given at $T \approx 10^4$ K. Thus, during the first moments of the plasma dynamics, the Stark contribution is necessarily underestimated. In our case, the experimental setup induces an apparatus function contribution greater than the Stark contribution for the Fe II transitions studied. As a result, the dependence of ω_{ki} on the temperature slightly affects the fidelity of the simulated emission spectra.

Fig. 20 illustrates the weak influence of the previous factors at long times. The figure details the comparison between the experimental spectrum and its simulation at time t = 950 ns.

Despite a Pearson correlation coefficient > 99.15%, the evolution with wavelength of the relative difference in spectral radiance $\Delta L_\lambda / L_\lambda$ highlights three spectral range for which the agreement is more or less satisfactory.

- On the [272.50, 273.75] nm spectral range: it seems difficult to perfectly simulate the Fe II 272.75 nm, Fe II 273.07 nm, Fe II 273.29 nm and Fe II 273.70 nm lines. The precision of the emission probabilities of these transitions (between 7% and 18%) explains the discrepancies between the experiment and the computation. On the other hand, several transitions observed experimentally are not tabulated in the databases (notably at 273.2 nm, 273.5 nm and 273.6 nm). We assume that these transitions correspond to the emission of Cr I or Cr II for which data available in literature are limited.
- On the [273.75, 275.75] nm spectral range (grayed on Fig. 20): the reconstruction is very satisfactory. The departures at 274.1 nm, 274.5 nm and around 275.2 nm can be ascribed to transitions not tabulated therefore excluded from the calculation or to convolution effects (apparatus function).
- On the [275.75, 277.00] nm spectral range: the main departures observed result from the Cr II 275.77 nm, Cr II 276.26 nm and Cr II 276.65 nm lines whose spectral data used for the modeling are theoretical [60] owing to the lack of available experimental information [24].

Table 6
Parameters used for the reconstruction of Fig. 21 with a two-layers approach.

t (ns)	ℓ_2/ℓ_1	n_{e2}/n_{e1}	T_2/T_1	p_2/p_1
50	0.1	4.22×10^{-3}	0.235	5.00
150	0.1	4.44×10^{-3}	0.242	7.14

3.9. Plasma uniformity and line reversal

Even if this section does not directly deal with the validation, the results presented here are discussed because they illustrate the ability of MERLIN to reproduce situations with $\ell_2 \neq 0$. We focus our attention on times t = 50 and 150 ns. The spectra shown for instance on Fig. 21 around 706 nm reveals the presence of a depletion located at a wavelength corresponding to the Ar I 706.72 nm transition without Stark shift despite the very high level of electron density. We can see at t = 150 ns the emission of this line redshifted by around 0.2 nm. This means that emission takes place in the conditions of the plasma with ℓ_1 and is absorbed beyond by argon at lower electron temperature and density. This characteristic is actually observed for the transitions of Ar I between 696 and 715 nm. This line reversal is due to the cold edge of the plasma containing a sufficient density in argon on the lower state of the related transitions. The reconstruction of the spectra therefore requires to consider a second layer with the thickness ℓ_2.

Using Eq. (21), spectra have been obtained from the following assumptions. The central plasma is characterized by parameters determined above (Sections 3.4 and 3.5). The thickness ℓ_2 of the cold layer is arbitrarily chosen such as $\ell_2 = 0.1\ell_1$. Its composition is assumed to be the same as the one of the central plasma. This hypothesis is strong since the cold layer corresponds to argon shocked by the hypersonic expansion of the central plasma. However, this layer may contain metallic elements in unknown proportions. Table 6 lists the physical quantities used to derive Fig. 21 where only Ar I transitions have been considered (see [24,51]). Fig. 21 also gives the relative difference in spectral radiance. In addition to the previous assumptions, the discrepancies can be ascribed to metallic transitions not taken into account.

Beyond the values of ℓ_2, n_{e_2} and T_2 which are not experimentally determined, MERLIN proves its ability to reconstruct the experimental signal by considering the ratios of Table 6. These orders of magnitude are consistent with other simulations of two-layer plasma emission [63]. At times t = 50 and 150 ns, the pressure p_2 in the peripheral

Table A.1
Constants used in the paper.

Constant	Meaning	Unit
c	Celerity of light in vacuum	2.997924×10^{8} m s^{-1}
e	Elementary Charge	1.602176×10^{-19} C
h	Planck constant	6.626070×10^{-34} J s
$\hbar$	Reduced Planck constant	1.05457×10^{-34} J s
k_B	Boltzmann constant	1.380649×10^{-23} J K^{-1}
m_e	Mass of the electron	9.1094×10^{-31} kg
ϵ_0	Vacuum dielectric permittivity	8.854187×10^{-12} m^{-3} kg^{-1} s^{4} A^{2}
π	Number pi	3.141592653589793

cold layer is $\approx 10^7$ Pa and $\approx 5 \times 10^6$ Pa, respectively. These values are in good agreement with a state-to-state modeling coupled with an Eulerian propagation approach of a laser-induced metallic plasma in an Ar environment developed by the team some years ago [64].

4. Conclusion

This paper has described the MERLIN code based on the resolution of the radiative transfer equation to simulate the experimental emission spectra of a laser-induced plasma on Eurofer97 steel in argon. The thermo-physical parameters of the calculations allowing the best agreement between the experimental and the computed spectra correspond to experimental measurements whose uncertainty has been evaluated. Therefore, no input quantity acts here as an adjustment parameter in the validation protocol. The departures between experiment and model are systematically linked to spectral and/or broadening data. If the code, in its current version, can lead to model the emission spectra of a wide variety of complex mixtures, its development is far from being complete. Indeed, we are currently implementing the sources of broadening not considered so far in order to reduce the hypotheses. The polynomial correlation for estimating the default Stark impact factor will soon be replaced by a more realistic general theoretical approach. In addition to extending the capabilities of this code to molecular spectra calculations, we are currently also working on building a spectral and Stark database built in SQL in order to no longer depend on online data availability. Finally, the outputs of this code are currently used for training deep neural networks to obtain generalized direct quantification models by supervised learning [65].

CRediT authorship contribution statement

Aurélien Favre: Writing – original draft, Software, Methodology, Investigation, Formal analysis, Conceptualization. **Arnaud Bultel:** Resources, Formal analysis. **Vincent Morel:** Software. **Morgan Lesage:** Software. **Léo Gosse:** Investigation.

Declaration of competing interest

The authors declare that they have no known competing financial interests or personal relationships that could have appeared to influence the work reported in this paper.

Acknowledgments

This work has been carried out within the framework of the French Federation for Magnetic Fusion Studies (FR-FCM) and of the EUROfusion consortium, and has received funding from the Euratom research and training programme 2019–2023 under grant agreement No 633053. The views and opinions expressed herein do not necessarily reflect those of the European Commission. The work has been also carried out within the framework fo the TITANS project under grant No 101059408 funded by the European Union. Views and opinions expressed are however those of the authors only and do not necessarily reflect those of the European Union. The authors also thank the "Agence Nationale de la Recherche" (ANR, France) through the program "Investissement d'Avenir" (ANR-10-LABX-09-01), LabEx EMC 3 having supported the PTOLEMEE and QUANTIPHY projects. This work has been also partially financed by the European Regional Development Fund (ERDF) of the European Union and by the "Région Normandie", France.

Appendix A

See Tables A.1–A.3.

Table A.2
Novel variables used in the paper.

Variable	Meaning	Unit
A_S	Stark broadening parameter of ionic origin	
a	Self-absorption power law coefficient No 1	
A_{ki}	Probability of spontaneous emission of the transition $k \rightarrow i$	s^{-1}
b	Self-absorption power law coefficient No 2	
C_1	Electron-ion continuum constant	W m^{4} K$^{0.5}$ sr^{-1}
C_2	Electron-neutral continuum constant	W m^{2} K$^{-1.5}$ sr^{-1}
C_6	VDW expansion constant	m^{6} s^{-1}
C_{ki}^{SA}	Self-absorption Correction coefficient of the transition $k \rightarrow i$	
D_i	Ionization degree of plasma	
E_{di}	Dissociation energy	eV
E_{io}	Ionization energy	eV
E_{io}^{c}	Ionization energy corrected by potential reduction	eV
E_k	Energy of starting level k	eV
f_e	Spectrometer entrance slit width	m
f_{i0}	Oscillator strength of transition $i \rightarrow 0$ (fundamental)	
g_k	Degeneracy of starting level k	
$g_0^{X^{(Z+)}}$	Degeneracy of the fundamental level of the ion $X^{(Z+)}$	
L_{ki}	Transition radiance $k \rightarrow i$ (thick opt.)	W m^{-2} sr^{-1}
L_{ki}^{OT}	Transition radiance $k \rightarrow i$ (thin opt.)	W m^{-2} sr^{-1}
K_{eq}	Equilibrium constant of a reaction	m^{-3}
k_f	Forward reaction rate	m^{3} s^{-1}

(*continued on next page*)

Table A.2 (*continued*).

Variable	Meaning	Unit
k_b	Backward reaction rate	$m^6\ s^{-1}$
ℓ_1	Thickness of the core of the emitting plasma	m
ℓ_2	Thickness of the cold layer peripheral to the emitting plasma	m
L_λ	Spectral radiance	W m^{-2} sr^{-1} m^{-1}
$L_{\lambda,T}$	Equilibrium spectral radiance of a uniform LIP	W m^{-2} sr^{-1} m^{-1}
$L^0_{\lambda,T}$	Black body spectral radiance at temperature T	W m^{-2} sr^{-1} m^{-1}
N_D	Number of particles in the Debye sphere	
N_X	Number of particles of the species X	
n_e	Electron density	m^{-3}
n_{e2}	Electron density of the peripheral cold layer	m^{-3}
$n_{e,r}$	Reference electron density	m^{-3}
n_{tot}	Total plasma density	m^{-3}
n_X	Density of element X	m^{-3}
$n_{X\ I}$	Density of neutral element X	m^{-3}
p	Pressure	Pa
p_2	Pressure in the cold layer peripheral to the emitting plasma	Pa
p_i	Pressure of charges associated with plasma ions	Pa
Q_X	Partition function of the species X (*see context*)	
T	Temperature	K
T_2	Temperature of the cold layer peripheral to the emitting plasma	K
t	Plasma time (*see context*)	s
V	Plasma volume	m^3
x_X	Mole fraction of the element X in the LIP	
$x_X{}^*$	Mole fraction of the element X in the sample	
$[X_0]$	Population density of level 0 (fundamental) of the specie X	m^{-3}
$[X_k]$	Population density of level k of the specie X	m^{-3}
y_{ℓ_1}	Relief ordinate for the measurement of ℓ_1	
Z	State of charge or ionization level	

Table A.3
Greek variables used in the paper.

Variable	Meaning	Unit
α_λ	Absorption coefficient	m^{-1}
β	Stark broadening ionic contribution factor	
Γ	Spectral profile	m^{-1}
ΔE_{io}	Ionization potential reduction	eV
$\Delta\lambda_{1/2,G}$	Gaussian FWHM	m
$\Delta\lambda^D_{1/2,G}$	Doppler FWHM	m
$\Delta\lambda^A_{1/2,L}$	Instrumental FWHM	m
$\Delta\lambda^R_{1/2,L}$	Resonance FWHM	m
$\Delta\lambda^S_{1/2,L}$	Stark FWHM	m
$\Delta\lambda^V_{1/2,L}$	Van der Waals FWHM	m
$\delta_{i,j}$	Kronecker symbol	
δ_λ	Volume spectral diffusion coefficient	W m^{-3} sr^{-1} m^{-1}
$\delta_{\lambda_{ki}}$	Electronic shift factor of the transition $k \to i$	m
ϵ_λ	Emission coefficient	W m^{-3} sr^{-1} m^{-1}
$\epsilon_{\lambda,X}$	Emission coefficient of the specie X	W m^{-3} sr^{-1} m^{-1}
$\epsilon^{cont}_{\lambda,X}$	Continuous emission coefficient of the element X	W m^{-3} sr^{-1} m^{-1}
$\epsilon^{ki}_{\lambda,X}$	Bound-bound emission coefficient of the element X	W m^{-3} sr^{-1} m^{-1}
$\epsilon^{fb}_{\lambda,X^{(Z+)}}$	Free-bound emission coefficient associated with $X^{(Z-1)+}$	W m^{-3} sr^{-1} m^{-1}
$\epsilon^{ff,ea}_{\lambda,X}$	Free-free emission coefficient of the element X	W m^{-3} sr^{-1} m^{-1}
$\epsilon^{ff,ei}_{\lambda,X^{(Z+)}}$	Free-free emission coefficient of the ion $X^{(Z+)}$	W m^{-3} sr^{-1} m^{-1}
ζ	Plasma dilution factor	
λ	Given or observed wavelength	m
λ_{i0}	Tabulated wavelength of the transition $i \to 0$ (fundamental)	m
λ_{ki}	Tabulated wavelength of the transition $k \to i$	m
μ	Reduced mass	kg
ξ^{fb}	Bibermann factor of free-bound interaction	
ξ^{ff}	Bibermann factor of free-free interaction	
ρ_λ	Spectral reflectivity	
τ_λ	Spectral transmissivity	
σ_{ea}	Electron-neutral interaction cross section	m^2
τ_{res}	Resolution characteristic time	s
$\Psi_\lambda(\overrightarrow{\Omega_1}, \overrightarrow{\Omega_2})$	Phase function of the directions $\overrightarrow{\Omega_1}$ and $\overrightarrow{\Omega_2}$	W^{-1} m^2 sr^2 m
ω_{ki}	Electronic impact factor of the transition $k \to i$	m

Data availability

Data will be made available on request.

References

[1] Paris P, Butikova J, Laan M, Hakola A, Jõgi I, Likonen J, et al. Comparison of LIBS results on ITER-relevant samples obtained by nanosecond and picosecond lasers. Nucl Mater Energy 2019;18:1–5. http://dx.doi.org/10.1016/j.nme.2018.11.018.

[2] Nishijima D, Doerner RP. Stark width measurements and Boltzmann plots of W I in nanosecond laser-induced plasmas. J Phys D: Appl Phys 2015;48:325201. http://dx.doi.org/10.1088/0022-3727/48/32/325201.

[3] Cirisan M, Cvejić M, Gavrilović MR, Jovićević S, Konjević N, Hermann J. Stark broadening measurement of Al II lines in a laser-induced plasma. J Quant Spectrosc Radiat Transfer 2014;133:652–62. http://dx.doi.org/10.1016/j.jqsrt.2013.10.002.

[4] Mercadier L, Hermann J, Grisolia C, Semerok A. Diagnostics of nonuniform plasmas for elemental analysis via laser-induced breakdown spectroscopy: demonstration on carbon-based materials. J Anal At Spectrom 2013;28(1446). http://dx.doi.org/10.1039/c3ja50127b.

[5] Kramida A, Olsen K, Ralchenko Y. NIST lIBS database (ver. 5.10). Gaithersburg, MD: National Institute of Standards and Technology - Atomic Spectroscopy Group and Quantum Measurement Division; 2024, https://physics.nist.gov/PhysRefData/ASD/LIBS/libs-form.html.

[6] Goldenstein CS, Miller VA, Spearrin RM, Strand CL. SpectraPlot.com: Integrated spectroscopic modeling of atomic and molecular gases. J Quant Spectrosc Radiat Transfer 2017;200:249–57. http://dx.doi.org/10.1016/j.jqsrt.2017.06.007.

[7] Laux C, Spence TG, Kruger CH, Zare RN. Optical diagnostics of atmospheric pressure air plasmas. Plasma Sources Sci Technol 2003;12:125–38. http://dx.doi.org/10.1088/0963-0252/12/2/301.

[8] Pannier E, Laux C. RADIS: A nonequilibrium line-by-line radiative code for CO2 and HITRAN-like database species. J Quant Spectrosc Radiat Transfer 2019;222–223:12–25. http://dx.doi.org/10.1016/j.jqsrt.2018.09.027.

[9] Luque J, Crosley DR. LIFBASE: Database and spectral simulation program (version 1.5). SRI international report MP, 99 009, 1999.

[10] Western CM. PGOPHER: A program for simulating rotational, vibrational and electronic spectra. J Quant Spectrosc Radiat Transfer 2017;186:221–42. http://dx.doi.org/10.1016/j.jqsrt.2016.04.010.

[11] Veis P, Marin-Roldan A, Dwivedi V, Karhunen J, Paris P, Jogi I, et al. Quantification of H/D content in Be/W mixtures coatings by CF-LIBS. Phys Scr T 2020;171:014073. http://dx.doi.org/10.1088/1402-4896/ab7ebd.

[12] Favre A, Morel V, Bultel A, Godard G, Idlahcen S, Benyagoub A, et al. Double pulse laser-induced plasmas on W and Al by ps-LIBS: Focus on the plasma-second pulse interaction. Fus Eng Des 2021;168:112364. http://dx.doi.org/10.1016/j.fusengdes.2021.112364.

[13] Favre A, Morel V, Bultel A, Godard G, Idlahcen S, Diez M, et al. Interface detection by picosecond Laser-Induced Breakdown Spectroscopy (LIBS): Application to a physical vapor deposited tungsten layer on a copper-chromium-zirconium substrate. Opt Laser Technol 2022;150:107913. http://dx.doi.org/10.1016/j.optlastec.2022.107913.

[14] Favre A, Bultel A, Lamine Sankhe M, Vartanian S, Bruno V, Morel V, et al. A step towards the diagnostic of the ITER first wall: in-situ LIBS measurements in the WEST tokamak. Phys Scr 2024;3(99):035609. http://dx.doi.org/10.1088/1402-4896/ad2826.

[15] Favre A, Bultel A, Payet M, Vartanian S, Garcia-Argote S, Morel V, et al. LIBS analysis of tritium in thin film-type samples. J Nucl Mater 2024;591:154924. http://dx.doi.org/10.1016/j.jnucmat.2024.154924.

[16] Morel V, Favre A, Bultel A, Gosse L, Lacour C, Coppalle A. Determination of the composition of biomass pellets (wood, grass and agricultural residues) by means of CF-LIBS. Spectrochim Acta B 2024 [submitted for publication].

[17] Drawin HW. In: Rompe R, Steenbeck M, editors. Validity conditions for Local thermodynamic equilibrium, progress in plasmas and gas electronics. vol. 1, 1975.

[18] Alberti RA. Relation between the thermodynamics and kinetics of a complex reaction system at constant temperature and pressure. J Phys Chem 1991;95:413–7. http://dx.doi.org/10.1021/j100154a072.

[19] Stewart JC, Pyatt Jr, Kedar D. Lowering of ionization potentials in plasmas. Astrophys J 1966;144:1203–11. http://dx.doi.org/10.1086/148714.

[20] Unsöld A. Quantitative spektralanalyse der sonnenatmosphäre. Z Astrophys 1948;24:306–9, SAO/NASA Astrophysics Data System.

[21] Ecker G, Kröll W. Lowering of the ionization energy for a plasma in thermodynamic equilibrium. Phys Fluids 1963;6(1):62–9. http://dx.doi.org/10.1063/1.1724509.

[22] Griem HR. High-density corrections in plasma spectroscopy. Phys Rev 1962;128(3):997–1003. http://dx.doi.org/10.1103/PhysRev.128.997.

[23] Prenzel R, Bornath Th, Schlanges M. Ionization and recombination rates of dense carbon plasmas. Phys Lett A 1996;223(6):453–7. http://dx.doi.org/10.1016/S0375-9601(96)00764-5.

[24] Kramida A, Ralchenko Y, Reader J, NIST ASD team. NIST atomic spectra database (ver. 5.10). Gaithersburg, MD: National Institute of Standards and Technology; 2022, https://physics.nist.gov/asd.

[25] Capitelli M, Colonna G, Giordano D, Marraffa L, Casavola A, Minelli P, Pagano D, et al. Tables of internal partition functions and thermodynamic properties of high-temperature mars-atmosphere species from 50k to 50000k, 246. 2005, ESA STR-246.

[26] Bultel A, Chéron BG, Bourdon A, Motapon O, Schneider IF. Collisional-radiative model in air for earth re-entry problems. Phys Plasmas 2006;13:043502. http://dx.doi.org/10.1063/1.2194827.

[27] Annaloro J. Modèles collisionnels-radiatifs appliqués aux situations d'entrée atmosphériques martienne et terrestre [Ph.D. thesis], France: University of Rouen; 2013.

[28] Snyder C, McBride BJ, Zehe MJ, Gordon S. NASA Glenn's chemical equilibrium with applications (CEA) code. OH United States: NASA Glenn Research Center; 2022, https://cearun.grc.nasa.gov/.

[29] Gleizes A, Gonzalez JJ, Freton P. Thermal plasma modelling. J Phys D: Appl Phys 2005;38(9):R153–83. http://dx.doi.org/10.1088/0022-3727/38/9/r01.

[30] Wilbers ATM, Kroesen GMW, Timmermans CJ, Schram DC. The continuum emission of an arc plasma. J Quant Spectrosc Radiat Transfer 1991;45(1):0022–4073. http://dx.doi.org/10.1016/0022-4073(91)90076-3.

[31] Venugopalan M. Reactions under plasma conditions. Wiley; 1971, p. 367–469, Cabannes & Chapelle, Chap. 7.

[32] Devoto RS. Transport coefficients of ionized argon. Phys Fluids 1973;5(16):616–23. http://dx.doi.org/10.1063/1.1694396.

[33] Sutherland RS. Accurate free-free gaunt factors for astrophysical plasmas. Mon Not R Astron Soc 1998;2(300):321–30. http://dx.doi.org/10.1046/j.1365-8711.1998.01687.x.

[34] Ida T, Ando M, Toraya H. Extended pseudo-Voigt function for approximating the Voigt profile. J Appl Crystallogr 2000;33:1311–6. http://dx.doi.org/10.1107/S0021889800010219.

[35] Liu Y, Lin J, Huang G, Guo Y, Duan C. Simple empirical analytical approximation to the Voigt profile. J Opt Soc Am B 2001;5(18):666–72. http://dx.doi.org/10.1364/JOSAB.18.000666.

[36] Sanchez-Bajo F, Cumbrera FL. The use of the pseudo-Voigt function in the variance method of X-ray line-broadening analysis. J Appl Crystallogr 1997;30:427–30. http://dx.doi.org/10.1107/S0021889896015464.

[37] Wertheim GK, Butler MA, West KW, Buchanan DNE. Determination of the Gaussian and Lorentzian content of experimental line shapes. Rev Sci Instrum 1974;11(45):1369–71. http://dx.doi.org/10.1063/1.1686503.

[38] Quinet P, Fivet V, Palmeri P, DESIRE Team. DatabasE on SIxth Row Elements. 2022, https://hosting.umons.ac.be/html/agif/databases/desire.html.

[39] Kunze HJ. Introduction to plasma spectroscopy. 2009, http://dx.doi.org/10.1017/CBO9781107415324.004, arXiv:1011.1669v3.

[40] Laux C. Optical diagnostics and radiative emission of air plasmas. California: Stanford University; 1993, 1993PhDT.....206L.

[41] Kelleher DE. Stark broadening of visible neutral helium lines in a plasma. J Quant Spectrosc Radiat Transfer 1981;3(25):191–220. http://dx.doi.org/10.1016/0022-4073(81)90089-3.

[42] Konjević N. Plasma broadening and shifting of non-hydrogenic spectral lines: present status and applications. Phys Rep 1999;6(316):339–401. http://dx.doi.org/10.1016/S0370-1573(98)00132-X.

[43] Griem HR. Spectral line broadening by plasmas. Academic Press; 1974.

[44] Nikiforov AY, Leys C, Gonzalez MA, Walsh JL. Electron density measurement in atmospheric pressure plasma jets: Stark broadening of hydrogenated and non-hydrogenated lines. Plasma Sources Sci Technol 2015;24:034001. http://dx.doi.org/10.1088/0963-0252/24/3/034001.

[45] Oks EA, Galdetskii AV. Quasi-static stark profiles of hydrogen lines broadened by plasma turbulence. Izvestiya Ordena Trudovogo Krasnogo Znameni Krymskoj Astrofizicheskoj Observatorii 1982;65:59–71.

[46] Fantoni R, Almaviva S, Caneve L, Colao F, Maddaluno G, Gasior P, et al. Hydrogen isotope detection in metal matrix using double-pulse laser-induced breakdown-spectroscopy. Spectrochim Acta B 2017;1(129):8–13. http://dx.doi.org/10.1016/j.sab.2016.12.008.

[47] Farid N, Li C, Wang H, Ding H. Laser-induced breakdown spectroscopic characterization of tungsten plasma using the first, second, and third harmonics of an Nd:YAG laser. J Nucl Mater 2013;1–3(433):80–5. http://dx.doi.org/10.1016/j.jnucmat.2012.09.002.

[48] Kononenko TV, Garnov SV, Klimentov SM, Konov VI, Loubnin EN, Dausinger F, et al. Laser ablation of metals and ceramics in picosecond-nanosecond pulsewidth in the presence of different ambient atmospheres. Appl Surf Sci 1997;109–110:109–10. http://dx.doi.org/10.1016/S0169-4332(96)00905-1.

[49] Hermann J, Grojo D, Axente E, Gerhard C, Burger M, Craciun V. Ideal radiation source for plasma spectroscopy generated by laser ablation. Phys Rev E 2017;96:1–6. http://dx.doi.org/10.1103/PhysRevE.96.053210.

[50] Montupet-Leblond F, Corso L, Payet M, Delaporte-Mathurin R, Bernard E, Charles Y, et al. Permeation and trapping of hydrogen in Eurofer97. Nucl. Mater. Energy 2021;29:101062. http://dx.doi.org/10.1016/j.nme.2021.101062.

[51] Konjević N, Lesage A, Fuhr JR, Wiese WL. Experimental Stark widths and shifts for spectral lines of neutral and ionized atoms (A critical review of selected data for the period 1989 through 2000). J Phys Chem Ref Data 2002;31(3):819–927. http://dx.doi.org/10.1063/1.1486456.

[52] Mijatović Z, Djurović S, Gavanski L, Gajo T, Favre A, Morel V, et al. Plasma density determination by using hydrogen Balmer Hα spectral line with improved accuracy. Spectrochim Acta B 2020;166:105821. http://dx.doi.org/10.1016/j.sab.2020.105821.

[53] Büscher S, Wrubel Th, Ferri S, Kunze H-J. The Stark width and shift of the hydrogen H_α line. J Phys B: At Mol Opt Phys 2002;35(13):2889–97. http://dx.doi.org/10.1088/0953-4075/35/13/304.

[54] El Sherbini AM, El Sherbini Th M, Hegazy H, Cristoforetti G, Legnaioli S, Palleschi V, et al. Evaluation of self-absorption coefficients of aluminum emission lines in laser-induced breakdown spectroscopy measurements. Spectrochim Acta B 2005;12(60):1573–9. http://dx.doi.org/10.1016/j.sab.2005.10.011.

[55] Hermann J, Axente E, Craciun V, Taleb A, Pelascini F. Evaluation of pressure in a plasma produced by laser ablation of steel. Spectrochim Acta B 2018;143:63–70. http://dx.doi.org/10.1016/j.sab.2018.02.015.

[56] Safi A, Tavassoli SH, Cristoforetti G, Legnaioli S, Palleschi V, Rezaei F, et al. Determination of excitation temperature in laser-induced plasmas using columnar density Saha-Boltzmann plot. J Adv Res 2019;18:1–7. http://dx.doi.org/10.1016/j.jare.2019.01.008.

[57] Zhang ZM, Chen S, Liang YZ. Baseline correction using adaptive iteratively reweighted penalized least squares. Analyst 2010;135:1138–46. http://dx.doi.org/10.1039/B922045C.

[58] Peacock RN. Practical selection of elastomer materials for vacuum seals. J Vac Sci Technol 1980;17(330). http://dx.doi.org/10.1116/1.570380.

[59] Edwards Jr. D. An upper bound to the outgassing rate of metal surfaces. J Vac Sci Technol 1977;14(1030). http://dx.doi.org/10.1116/1.569315.

[60] Kurucz RL, Bell B. KURUCZ database, atomic line data no. 23. 2022, https://lweb.cfa.harvard.edu/amp/ampdata/kurucz23/sekur.html.

[61] Van H, Peter AM. Recent development of the atomic line list. Galaxies 2018;6. http://dx.doi.org/10.3390/galaxies6020063, https://www.pa.uky.edu/peter/newpage/.

[62] Wendt M. Net emission coefficients of argon iron plasmas with electron Stark widths scaled to experiments. J Phys D: Appl Phys 2011;44:125201. http://dx.doi.org/10.1088/0022-3727/44/12/125201.

[63] Hermann J, Lorusso A, Perrone A, Strafella F, Dutouquet C, Torralba B. Simulation of emission spectra from nonuniform reactive laser-induced plasmas. Phys Rev E 2015;92:053103. http://dx.doi.org/10.1103/PhysRevE.92.053103.

[64] Morel V, Bultel A, Schneider I, Grisolia C. State-to-state modeling of ultrashort laser-induced plasmas. Spectrochim Acta B 2017;127:7–19. http://dx.doi.org/10.1016/j.sab.2016.11.002.

[65] Favre A, Abad A, Poux A, Gosse L, Berjaoui A, Morel V, et al. Towards real-time calibration-free LIBS supported by machine learning. Spectrochim Acta B 2025 [in review].